Highlights

1. Detailed evaluation of mechanisms in the transesterification reaction medium
2. First time report of viscosity and density measurements for polar and non-polar phase in the biodiesel reaction medium
3. First time report of flow visualisation results of two phase flow in a tubular biodiesel reactor
4. Development of first multiphase CFD model for biodiesel reaction medium

Development and Validation of a two phase CFD model for tubular Biodiesel Reactors

Karne de Boer and Parisa A. Bahri[1]

School of Engineering and Information Technology, Murdoch University, Perth, Western Australia

Abstract

The use of biodiesel as an alternative to diesel has gained increasing momentum over the past 15 years. To meet this growing demand there is a need to optimise the transesterification reactor at the heart of the biodiesel production system. Assessing the performance of innovative reactors is difficult due to the liquid-liquid reaction mixture that is affected by mass transfer, reaction kinetics and component solubility. This paper presents a Computational Fluid Dynamic model of a tubular reactor developed in ANSYS CFX that can be used to predict the onset of mixing via turbulent flow. In developing the model an analysis of the reaction mixture is provided before the presentation of experimental data, which includes flow visualisation results and temperature dependant viscosity and density data for each phase. The detailed data and model development procedure represents an advancement in the modeling of the two phase transesterification reaction used in biodiesel production.

.

Keywords: Computational Fluid Dynamics, Two phase flow, Biodiesel, FAME, glycerol

1 Introduction

1.1 Biodiesel

Biodiesel, a fuel derived from vegetable oil or animal fat, is a direct petro-diesel replacement that can significantly reduce emissions and provide energy independence (Sheehan *et al.*, 1998). The main drivers for the rapid development of biodiesel has been increasing pressure on low cost oil supplies, greater public awareness of global warming and a strong desire to link the economic benefits of fuel production to the point of consumption.

[1] Corresponding author Email: p.bahri@murdoch.edu.au

With greater demand for biodiesel, there has been greater demand for feedstock and a need to optimise the production process. The central unit operation in the biodiesel production process is the transesterification reactor in which vegetable oils are chemically converted to biodiesel and glycerol through reaction with methanol and a suitable alkaline catalyst. This paper presents the application of Computational Fluid Dynamic (CFD) modeling techniques to a tubular biodiesel reactor to provide foundational information for its optimisation and development.

1.2 CFD Modeling

CFD modeling has been applied to biodiesel production processes to advance understanding of the physical and chemical processes that occur. Adeyemi *et al.,* (2013) used FLUENT to model transesterification in a 2L stirred reactor. In this work the reaction medium was modelled as a single phase with the transesterification modelled via kinetic rate equation linked to the component concentrations in the model elements. Wang *et al.,* (2012) developed a two phase flow and kinetic reaction model of canola oil hydrolysis in CFX which provided insight into the hydrolysis reaction. Due to the high temperatures considered in this work all phase data was estimated and not based on physical measurements. Wulandani *et al.,* (2012) developed a two phase model based on superheated methanol vapour contacting triglyceride droplets, however, no validation was provided. Orifici *et al.,* (2013) modelled the transesterification of palm oil in a plug flow reactor using kinetic rate data incorporated into a single phase model. To the best of the authors' knowledge there is no existing literature on the development of a two phase liquid-liquid model of the transesterification reaction, and as shown above all existing works are based on single phase flow. The work of Wang *et al.,* (2012*)* is a two phase work, however, it is focused on hydrolysis rather than transesterification.

The only other known publication in this area is an early conference paper published by the authors which shared the initial findings of the modeling work (de Boer and Bahri, 2009). The focus of this paper is to provide a detailed report on the model development process which includes evaluation of the multiphase reaction medium; determination of appropriate model inputs and investigation of suitable physical models to adequately simulate the

observed phenomena. The aim is to advance the application of CFD modeling tools in the field of biodiesel providing reference data for further work in this area.

Although specifically developed for tubular reactors, the core information presented in this paper can be applied to develop CFD models of any biodiesel reactor designs. Furthermore the foundational work conducted in this paper can assist in the development of CFD models of tubular reactors for other liquid-liquid reactions or flow conditions (e.g.: oil and water).

The model development process is based on a detailed review of the transesterification reaction. In light of this review, experimental data is presented that includes the viscosity and density of the two reacting phases and flow visualisation results in a pilot scale industrial reactor. The former is required as an input to the model and the latter used to qualitatively verify the CFD model. Details of the model implementation in ANSYS CFX 12 are then provided with the outputs subsequently compared to the flow visualisation results.

1.3 Biodiesel Reaction Medium

In a typical biodiesel reactor, oil or fat (triglyceride) is converted to Fatty Acid Methyl Esters (FAME) and a co-product glycerol via a catalysed chemical reaction (transesterification). The glycerol is then separated from the FAME with both products subsequently purified. The purified FAME are known as biodiesel while the purified glycerol is sold as a co-product.

It is widely accepted that the conversion of oil to FAME in the reactor proceeds via three consecutive reversible reactions (Noureddini and Zhu, 1997; Vicente *et al.*, 2005b):

$$\text{Triglyceride} + \text{Methanol} \overset{\text{Catalyst}}{\Leftrightarrow} \text{Diglyceride} + \text{FAME}$$

$$\text{Diglyceride} + \text{Methanol} \overset{\text{Catalyst}}{\Leftrightarrow} \text{Monoglyceride} + \text{FAME}$$

$$\text{Monoglyceride} + \text{Methanol} \overset{\text{Catalyst}}{\Leftrightarrow} \text{Glycerol} + \text{FAME}$$

The reactant intermediates (diglycerides and monoglycerides) appear in small concentrations during the reaction and are considered contaminants in the final product. Different catalysts have been investigated in this reaction, including homogeneous (liquid) (Vicente *et al.*, 2003), heterogeneous (solid) (Lotero *et al.*, 2006), enzymes (Akoh *et al.*, 2007) and even no catalyst at extreme conditions (de Boer and Bahri, 2011). Despite this wide variety of approaches, almost all commercial plants throughout the world currently use an alkaline homogeneous catalyst (sodium or potassium methylate) (Mittelbach and Remschmidt, 2006).

Investigations into the transesterification reaction have shown that it transitions from a biphasic liquid mixture (oil and methanol) to another biphasic mixture (FAME and glycerol) via a pseudo-single phase emulsion (Noureddini and Zhu, 1997; Stamenkovic *et al.*, 2007; Stamenkovic *et al.*, 2008). Throughout the reaction a continuous non-polar phase (Oil, FAME and reaction intermediates) and a dispersed polar phase (methanol, glycerol and catalyst) are present with the composition of the phases constantly changing. Due to the biphasic nature of the reaction medium the rate of reaction is affected by chemical kinetics, mass transfer and component solubility.

The kinetic rate constants for the three stepwise transesterification reactions have been determined by a number of researchers (Darnoko and Cheryan, 2000; Freedman *et al.*, 1986; Karmee *et al.*, 2006; Noureddini and Zhu, 1997; Vicente *et al.*, 2005b). These studies do not explicitly account for the heterogeneous nature of the reaction, consequently, mass transfer and solubility effects are incorporated into the rate constants (Doell *et al.*, 2008). Despite this common simplification, the reaction progression has been shown to be sigmoidal and can be characterised by three stages as shown in Figure 1. The first stage is characterised by an initial slow rate of reaction; the second by a rapid progression up to approximately 80% conversion and finally a third stage as equilibrium is approached (Noureddini and Zhu, 1997).

In the first stage, the concentration of oil in the methanol droplets (where the majority of the catalyst resides) is low, requiring significant agitation to reach saturation levels (Boocock *et al.*, 1996). During the first stage it is most likely that the rate of mass transfer between the

phases is slower than the rate of chemical reaction, thus mass transfer is the rate limiting factor (Noureddini and Zhu, 1997; Stamenkovic *et al.*, 2007).

In the second stage, the reaction rate rapidly increases. Stamekovic *et al.* (2007; 2008), observed that this increase coincided with a reduction in droplet size. As the droplet size decreases, the surface area of the polar phase and thus the mass transfer rate increases, explaining the sudden jump in reaction rate. The reaction medium during this stage has been described by some as a pseudo single phase emulsion (Ma *et al.*, 1999; Zhou and Boocock, 2006) . Different authors have attributed the self-enhanced mass transfer rate to the surfactant action of the reaction intermediates (Boocock *et al.*, 1998; Stamenkovic *et al.*, 2007), while others have attributed it to the solvent properties of FAME (Noureddini and Zhu, 1997).

In the third step, the reaction rate rapidly curtails as equilibrium is approached. It is proposed that this sudden fall is due to the breaking of the single phase emulsion as glycerol is formed, resulting in the catalyst preferentially dissolving in the polar phase. With almost all of the un-reacted glycerides residing in the non-polar phase this results in a very slow approach to equilibrium. It is therefore proposed that in the final stage, it is the solubility of components and not the rate of mass transfer which limits the reaction rate. This was also observed in the reverse reaction (glycerolysis of FAME) (Kimmel, 2004; 2006).

In most industrial operations the methanolysis reaction is conducted between 50°C and 70°C with significant mixing. Under these conditions it is reasonable to assume that the effect of mass transfer limitations in the first stage is negligible (Noureddini and Zhu, 1997; Vicente *et al.*, 2005a). In the second stage, the absence of mass transfer limitations allows the reaction to be treated as a single phase. Consequently, both the first and second stages of the reaction can be adequately described by second order kinetics models available in the literature that ignore the multiphase behaviour of the reaction.

This second order model could be extended to the third reaction step, however, the high difference in density can result in the glycerol laden polar phase separating from the non-

polar phase causing the reaction to cease prematurely. This is especially true for tubular reactors in which the flow can stratify on long straight runs with insufficient turbulence.

CFD modeling was identified as an excellent tool to investigate the flow behavior of the two phases in tubular reactors during the final stage of the reaction. The development of such a CFD model allows different reactor designs (diameter and length) and operating conditions (flow-rate) to be easily trialed. The remainder of this paper firstly introduces the experimental work conducted on a tubular reactor and secondly provides details on the CFD model developed to represent the biphasic flow in the reactor.

2 Experimental Method and Materials

For the purpose of developing the CFD model it was identified that viscosity and density data for both phases would be required as well as flow visualisation results to verify the outputs of the model.

2.1 Viscosity and Density

To measure the viscosity and density properties, a sample of the reaction medium was taken and allowed to settle. The viscosity and density of each phase were measured from 30°C to 70°C at 3°C or 5°C increments using a Stabinger viscometer. The viscosity measurements are reproducible to 0.35% of the measurement, and density measurements are reproducible to 0.0005g/cm^3. The temperature was maintained to within 0.005°C.

2.2 Flow Visualisation

To provide qualitative direction and validation for the CFD model, a novel high temperature and pressure tubular reactor developed by Bluediesel PTY LTD was used to conduct flow visualisation studies. The reactor consists of multiple straight runs (5.8m) followed by tight (180°) bends. Before the tubular reactor a mixing tank is present in which the first two stages of the reaction rapidly occur. As a result, the reactants typically enter the tubular reactor 80% reacted and thus in the final stage of the reaction.

To allow visualisation of the fluid flow, a 4m run of thick walled (2.5mm) borosilicate glass tube was plumbed into the midpoint of the reactor via three isolating valves. This tube had an

internal diameter of 11mm which was required to achieve a pressure rating in excess of 300 psi. Figure 2 depicts the experimental equipment with the thick lines representing the glass tube, the thin lines representing the stainless steel tube and the double vertical lines the unions between lengths. To record the flow visualisation results, a high resolution digital video camera was setup on a tripod adjacent to the glass tubing. This video camera was used to record the flow of the coloured liquid against a white backdrop.

3 Results

3.1 Viscosity and Density

Viscosity and density of the non-polar and polar phases of the canola and coconut reaction mixtures are shown in Tables 2 through to 5, respectively. Temperature correlations for density and viscosity are provided in Tables 6 and 7, respectively.

The results in Tables 2 to 5 show the viscosity and density decreasing with increasing temperature as expected. The density of the two non-polar phases (Tables 2 and 4) are very similar, while the viscosity is noticeably higher in the canola mixture because of the longer average carbon chain length of the fatty acids (Krisnangkura *et al.*, 2006).

The very different results for the two polar phases in Tables 3 and 5 can be attributed to the different methanol contents in the two experiments. In the first experiment (canola) the methanol content was higher as the reaction was originally charged with a high methanol to oil ratio and it was fresh. In the second experiment (coconut) the methanol content was low as it was originally charged with a low methanol to oil molar ratio (5:1) and it had been sitting for six months between the last use of the plant and the experimental run. The low methanol content in the coconut glycerol phase caused the density and viscosity measurements to be significantly higher than those for the canola glycerol phase.

3.1.1 Density

Variations of liquid density with temperature are commonly correlated using the linear relationship shown in Equation 1 (Coupland and McClements, 1997; Liew *et al.*, 1992). Where ρ, ρ_0 and ρ_1 are densities measured in kg/m^3 and T is temperature in degrees Celsius.

$$\rho = \rho_0 + \rho_1 T$$

Equation 1: Density correlation

Table 6 contains the linear correlations for the data shown in Tables 2 to 5; with the square of the residuals (R^2) confirming the linear correlation is a good fit for the data sets.

3.1.2 Viscosity

Liew *et al.,* (1992) correlated liquid viscosity with temperature using the relationship shown in Equation 2 (μ is viscosity, T is temperature, m,n and T_0 are correlation coefficients determined by fitting the curve to the data). This relationship was fitted to the data using the Fminsearch function in Matlab, which varied the three coefficients (m,n and T_0) to minimize the sum of the square of the errors (SSE). The values of the coefficients are shown in Table 7.

$$\log \mu = m + \frac{n}{T - T_0}$$

Equation 2: Viscosity correlation

These correlations were extrapolated to the reaction midpoint temperature (Table 1) for each experiment to provide the viscosity and density values shown in Tables 8 and 9.

3.2 Flow Visualisation

The flow visualisation results are summarised in Table 1, with the associated snapshots from the results videos contained in Figures 3 and 4, respectively (the full videos are available in the supplementary material). The results in the first row are for refined canola oil (<0.1% FFA) which was reacted with methanol at a ratio of 6:1 and a catalyst concentration (Potassium methylate) of 0.75% weight of oil. Food colouring (red, 50ml) was added to the mixing tank before the reactor to provide a clear distinction between the polar and non-polar phases.

The second row of Table 1 contains the experimental conditions for Refined Bleached Dried (RBD) coconut oil (Procter and Gamble, Australia) which had been reacted for a long period

of time with methanol at a ratio of 5:1 and catalyst concentration (Sodium Methylate) 0.5% weight of oil. Food colouring (green, 50ml) was added to the mixing tank before the reactor to provide a clear distinction between the polar and non-polar phase. The food colouring preferentially dissolves in the polar phase and provides a simple but effective method for multiphase flow visualisation (Zhou and Boocock, 2006).

The flow-rate was controlled using a variable speed drive on the high pressure pump that drove the reaction medium through the reactor. The superficial flow velocities for each case were calculated using the specific volumetric flow-rate of the pump (4.9L/Hz) and the tube diameter (0.011m).

Figures 3 and 4 contain snapshots taken from the visualisation results of experiments 1 and 2 shown in Table 1. In both cases there is a transition from horizontal stratified flow to dispersed flow. For the canola oil feedstock, the transition took place between 0.26 and 0.27m/s, while for the coconut oil feedstock the transition took place between 0.34 and 0.36 m/s. The significant difference in transition velocities can be attributed to the different methanol content in each case. The increased methanol content has a very limited co-solvency effect between the glycerol and methyl esters (Negi *et al.*, 2006), however, it significantly reduces the density and viscosity of the glycerol phase (see the difference in density between the canola and coconut glycerol phases in Tables 3 and 5, respectively). This effect reduces the turbulent energy required to disperse the polar phase into the non-polar phase and thus explains the lower velocity required to achieve dispersion in the canola based results.

It was observed that the transition from stratified to dispersed flow occurs via the propagation of longitudinal waves with wavelengths greater than the reactor diameter. This is the same mechanism that occurs in stratified water and oil flows with the crashing waves releasing droplets which leads to dispersion of the phases at increasing velocities (Al-Wahaibi and Angeli, 2007; Al-Wahaibi *et al.*, 2007). This is most clearly shown in the stills from 12Hz to 18Hz in experiment 2 (Figure 4) due to the clear distinction between phases.

4 Discussion

4.1 Flow Transition and Reynolds number

The flow visualisation results in Figures 3 and 4 demonstrate that the two-phase flow regime varies significantly with flow velocity. At low velocities, the flow stratifies while at higher velocities the polar phase becomes dispersed in the continuous non-polar phase. The first is undesirable as it limits mass transfer, while the second represents the intended design with each phase having access to the other and component solubility and reaction equilibrium being the only limitations in the final stage of reaction. When considering various tubular reactor designs (diameter and length) and operating conditions (flow-rate) it is necessary to predict the flow regime to prevent stratification.

In single phase flow, the dimensionless Reynolds number (Re), shown in Equation 3, is used to predict the onset of turbulent flow.

$$\mathrm{Re}_{\mathrm{TP}} = \frac{\rho_{\mathrm{m}} D_p U}{\mu_m}$$

Equation 3: Reynolds Number

To determine the Reynolds number for two phase flow (Re_{TP}) in a pipe (with diameter D_p), the volume averaged mixture densities (ρ_m) and viscosities (μ_m) were used as shown in Equation 4 andEquation 5. With the variables r_c and r_d being the volume fraction of the continuous and dispersed phases, respectively; the variables ρ_c and ρ_d being the densities of the continuous and dispersed phases, respectively and μ_c and μ_d being the viscosities of the continuous and dispersed phases, respectively. Typically the glycerol phase accounts for 15% of the reaction mixture volume and this value has been used in these calculations. The calculated Reynolds number for stratified, transition and dispersed flows for the two experiments are shown in Table 10.

$$\rho_{\mathrm{m}} = r_c \rho_c + r_d \rho_d$$

Equation 4: Volume averaged mixture density

$$\mu_m = r_c \mu_c + r_d \mu_d$$

Equation 5: Volume averaged mixture viscosity

Spriggs (1973) and many other authors suggest that true laminar flow exists below a Reynolds number of 2000, with a transition from laminar to turbulent flow between Reynolds numbers of 2000 and 3000. By examining the calculated results in Table 10 it is clear that this criterion provides a somewhat reasonable match with the transition to turbulent flow in this case, with numbers above 2000 corresponding with the polar phase being dispersed as recorded in Figures 3 and 4.

The use of Reynolds number provides a reasonable initial design estimate of the flow regime at a particular design velocity for tubular reactors. Unfortunately, the Reynolds number cannot capture the behaviour of the flow in more complex reactor geometries. The application of CFD modeling to this particular problem will provide further insight into the effect of reactor design on flow regime and a foundation for other more complicated reactor geometries.

5 CFD Model Development

There are two distinct approaches to modeling two phase flow, the first referred to as Eulerian-Langrangian and the second as Eulerian-Eulerian. In the former, the dispersed phase is treated as discrete particles that interact with the continuous phase, while in the latter both phases are modelled in the Eulerian framework with both having the same velocity in a defined control volume (mesh). The former, called Lagrangian particle tracking in ANSYS CFX 12, is suitable for low dispersed phase volume fractions, while the latter approach is suitable to higher dispersed phase volume fractions. The Eulerian-Eulerian approach was selected for the modeling of biodiesel reactors as the dispersed polar phase volume fraction remains virtually constant at 15% in the final stage of the reaction.

The model was setup as an inhomogeneous multiphase problem as each phase had its own flow field. In this approach simulation of the flow was carried out by solving the governing

equations of continuity and momentum conservation (Navier-Stokes Equations), which are shown in Equation 6 andEquation 7.

$$\frac{\partial r_i \rho_i}{\partial t} = \nabla.(r_i \rho_i \boldsymbol{U_i}) = 0$$

Equation 6: Continuity equation

Where ρ_i is the density of the respective phase, r_i the volume fraction of the phase and $\mathbf{U_i}$ is the mean velocity vector of the respective phase. There are no source terms in the continuity equation or interphase transfer terms as mass is not created or transferred between two phases.

$$\frac{\partial (r_i \rho_i \boldsymbol{U_i})}{\partial t} + \nabla.(r_i(\rho_i \boldsymbol{U_i} \otimes \boldsymbol{U_i}))$$

$$= -r_i \nabla \mathrm{p}_i + \nabla.(r_i \rho_i (\nabla \boldsymbol{U_i} + (\nabla \boldsymbol{U_i})^T))$$

$$= \mathrm{S}_{Mi} + \boldsymbol{M_i}$$

Equation 7: Momentum equation

Where S_{Mi} describes momentum sources due to external body forces (gravity and buoyancy) and M_i describes interfacial forces acting on phase i due to the presence of other phases. In this work the drag force ($F_{\alpha\beta}$), turbulent dispersion force ($\boldsymbol{F_C^{TD}}$), lift force ($\boldsymbol{F_C^{L}}$), virtual mass force ($\boldsymbol{F_C^{VM}}$) and wall lubrication force ($\boldsymbol{F_C^{WL}}$) are considered as shown in Equation 8.

$$\boldsymbol{M_i} = \boldsymbol{F_{\alpha\beta}} + \boldsymbol{F_C^{TD}} + \boldsymbol{F_C^{L}} + \boldsymbol{F_C^{VM}} + \boldsymbol{F_C^{WL}}$$

Equation 8: Forces acting on phases

The energy equation is not solved in this model as the reactor section under consideration is treated as isothermal.

As the flow is turbulent, the Reynolds decomposition is incorporated into the Navier Stokes equations, leading to the Reynolds Averaged Navier Stokes (RANS) equations (Versteeg and Malalsekera, 2007). The additional Reynolds stress terms in the RANS equations are calculated using a turbulence model. The industry standard two equation k-ε turbulence

model implemented in ANSYS CFX was used for this simulation as it is well suited to the flow regime present (ANSYS, 2009).

The physical properties (viscosity and density) for the non-polar and polar phases for the two experiments were taken from Tables 8 and 9, respectively. These were assumed to remain constant due to the isothermal operation of the reactor section under consideration.

The difference in density between the two phases necessitates the modeling of buoyancy. Buoyancy is modelled on the density difference of the two phases and results in the addition of a source term to the momentum equation ($S_M=(\rho- \rho_{ref})g$). The reference density was set equal to the continuous phase density to simplify the form of the momentum equation (ANSYS, 2009).

The transfer of momentum between phases is dependent on the interphase forces acting on the interfacial area per unit volume between phase α and β ($A_{\alpha\beta}$) (ANSYS, 2009). Due to the dispersed nature of the polar phase, the particle model was implemented in CFX which assumes the dispersed phase consists of sphere particles with a mean diameter d_β. This assumption allows the interfacial area to be calculated from the volume fraction (r_β) according to Equation 9:

$$A_{\alpha\beta} = \frac{6r_\beta}{d_\beta}$$

Equation 9: Interfacial area between phases (ANSYS, 2009)

The mean droplet diameter (d_β) for the polar phase was set as 0.055mm on the basis of the work of Stamenkovic *et al.,* (2007; 2008) in which experimental measurement showed a constant value between 0.05 and 0.06mm in the final stage of the reaction.

The major determinant of multiphase flow behaviour is the interphase momentum transfer, which is determined by the action of the interphase forces on the interfacial area (see Equation 8). The interfacial force between the phases is the sum of independent physical factors including the:

- Drag force
- Turbulent dispersion force
- Lift force
- Virtual mass force
- Wall lubrication force, and

The models used to implement these in ANSYS CFX are discussed below.

5.1.1 Drag Force

According to the work of Stanbridge and Sullivan (1999) and Hussain (2004) the drag force is the most influential interphase force in dispersed fluid flow. In ANSYS CFX the interphase drag force acting on phase α due to phase β is:

$$\boldsymbol{F}_{\alpha\beta} = c_{\alpha\beta}\left(\boldsymbol{U}_{\beta} - \boldsymbol{U}_{\alpha}\right)$$

Equation 10: Drag force per unit volume

Where $\boldsymbol{F}_{\alpha\beta}$ is the drag force per unit volume between phases α and β, **U** is the Velocity vector of phases α and β and $c_{\alpha\beta}$ is the drag coefficient which is determined from the dimensionless drag coefficient C_D, particle diameter (d) and volume fraction of the dispersed phase (r_β):

$$c_{\alpha\beta} = \frac{3C_D}{4d} r_\beta \rho_\alpha \left|\boldsymbol{U}_{\beta} - \boldsymbol{U}_{\alpha}\right|$$

Equation 11: ANSYS drag coefficient

Numerous drag models for the dimensionless drag coefficient (C_D) are available in CFX. In this model it was decided that the densely distributed Ishii-Zuber drag model be implemented

as this has precedent in other oil-water multiphase simulations (Hussain, 2004) and is applicable to general fluid particles (ANSYS, 2009). The densely distributed Ishii-Zuber correlation is shown in Equation 12.

$$C_D(Sphere) = \frac{24}{Re_m}(1 + 0.15Re_m^{0.687})$$

$$Re_m = \frac{\rho_c |\boldsymbol{U}_d - \boldsymbol{U}_c| d_p}{\mu_m}$$

$$\mu_m = \mu_c(1 - \frac{r_d}{r_{dm}})^{-2.5 r_{dm} \mu^*}$$

$$\mu^* = \frac{\mu_d + 0.4\mu_c}{\mu_d + \mu_c}$$

Equation 12: Ishii Zuber (densely distributed model) (ANSYS, 2009)

This model is similar to the Schiller Naumann drag model (ANSYS, 2009) which is based on the drag law for a single sphere. For a single sphere the drag coefficient is 24/Particle Reynolds number (Re_p) for low particle Reynolds number and a constant 0.44 above this level. The main difference with the Ishii Zuber model is that a mixture viscosity is used (see Equation 12). $\mathbf{U}_d$ and $\mathbf{U}_c$ are the velocity vectors for the dispersed and continuous phases respectively, R_m is the mixture Reynolds number, ρ_c is the continuous phase density, μ_c , μ_d and μ_m are the viscosities of the continuous phase, dispersed phase and the mixture respectively. While r_d is the volume fraction of the dispersed phase and r_{dm} is defined as the maximum packing value, which is defaulted to unity for a dispersed phase.

5.1.2 Turbulent Dispersion Force

The turbulent dispersion force models the dispersion of the polar phase from areas of high concentration to low concentration due to the turbulent eddies in the continuous phase (Burns *et al.*, 2004). In ANSYS CFX this can be implemented using the Favre averaged model (Equation 13) or the Lopez de Bertodano force (Equation 14). The turbulent dispersion force is highly dependent on the drag between the two phases.

$$F_c^{TD} = -F_d^{TD} = C_{TD} C_{cd} \frac{v_{tc}}{\sigma_{tc}} \left(\frac{\nabla r_d}{r_d} - \frac{\nabla r_c}{r_c} \right)$$

Equation 13: Favre averaged model (ANSYS, 2009)

C_{TD} is a user-modifiable CEL multiplier (default value is 1), C_{cd} is the momentum transfer coefficient for the interphase drag force, σ_{tc} is the turbulent Schmidt number for continuous phase volume fraction, taken as 0.9 and v_{tc} is the kinematic visocisity of the continuous phase.

$$M_c^{TD} = -M_d^{TD} = -C_{TD} \rho_c k_c \nabla r_c$$

Equation 14: Lopez de Bertodano model (ANSYS, 2009)

Where C_{TD} is a user defined constant, typically between 0.1 and 0.5, ρ_c is the continuous phase density, k_c is the turbulent kinetic energy and the final term is the gradient of the continuous phase volume fraction.

5.1.3 Lift force

The lift force acts in a direction perpendicular to the direction of relative motion of the two phases (ANSYS, 2009). The lift force is strongly dominated by the slip velocity between the phases and the curl of the continuous velocity (see Equation 15). The limited rotational flow phenomena in the tube suggests that this force will have a minimal effect as was observed by Hussain (2004).

$$F_c^L = r_d \rho_c C_L (\boldsymbol{U}_d - \boldsymbol{U}_c) \times curl(\boldsymbol{U}_c)$$

Equation 15: Lift Force (ANSYS, 2009)

Where r_d is the dispersed phase volume fraction, ρ_c is the continuous phase density, C_L is the non-dimensional lift coefficient and $\mathbf{U}_d$ and $\mathbf{U}_c$ are the velocity vectors of the dispersed and continuous phases respectively.

5.1.4 Virtual mass force

When a dispersed phase particle accelerates relative to the continuous phase, some part of the surrounding continuous phase is also accelerated. This extra acceleration of the continuous phase has the effect of added mass or added inertia (Ranade, 2002). As a result, the force associated with this phenomenon is referred to as the virtual mass force. This force is directly

proportional to the relative acceleration between the two phases (bracketed terms in Equation 16). In this model it was expected that this force would have a limited impact on the simulation as the dispersed phase is carried along in the continuous phase.

$$F_C^{VM} = r_d \rho_c C_{VM} \left(\frac{d_d \mathbf{U}_d}{dt} - \frac{d_c \mathbf{U}_c}{dt} \right)$$

Equation 16: Virtual mass force (ANSYS, 2009)

Where r_d is the dispersed phase volume fraction, ρ_c is the continuous phase density, C_{VM} is the virtual mass coefficient and $\mathbf{U}_d$ and $\mathbf{U}_c$ are the velocity vectors of the dispersed and continuous phases respectively.

5.1.5 Wall lubrication force

The wall lubrication force is intended to model the phenomena observed when bubbles concentrate close but not immediately adjacent to walls. This is particularly applicable to air bubbles in liquid flow and has been shown to have little effect in previous liquid-liquid flow work (Hussain, 2004).

With this background a base case simulation was developed to be a basis for systematic parametric investigation – the inputs for this base case are summarised in Table 11. The surface tension coefficient mentioned in this table was required for the Ishii-Zuber correlation and was taken from Allen (1999).

The boundary conditions for this base case are summarised in Table 12. For the studies performed, the inlet turbulence intensity was set at 5% which is typical for pipe flows (Abraham *et al.*, 2008). The outlet pressure was set at 20 psi.

5.1.6 Geometry, mesh and solver control

The flow domain of the biodiesel reactor was developed in ANSYS Design Modeller by extruding a sketch with the internal diameter (11mm) of the reactor tube. This flow domain mimics the experimental setup. A three dimensional mesh of this flow domain was developed

using the ANSYS meshing tool in Workbench 12. The nature of the tube lends itself to sweep meshing with the level of refinement determined by the face mesh controls and the number of sweep divisions. A mesh independence study was conducted for both pure tetrahedral face meshes and tetrahedral meshes with inflation at the tube walls (de Boer, 2010). The study resulted in the choice of the mesh shown in Figure 5 that gave reasonable solution times with high accuracy. Further refinement provided negligible increases in resolution of the base case for substantial increases in solution time. Details of the meshing parameters are summarised in Table 13.

The level of mesh refinement is also affected by the number of sweep divisions in the mesh (these determine the thickness of the face mesh cells throughout the volume). To minimise solution time 200 divisions was used for the 4m tube geometry. To further reduce computational time, tubes are typically split in half and a symmetry plane is inserted (Hussain, 2004). This halves the number of control volumes and therefore essentially halves the number of equations to be solved at each iteration. It was found that the use of a symmetry plane had minimal effect on the solution (de Boer, 2010) and as a result a half tube was modelled to cut the solution time in half. Using the mesh with the face pattern shown in Figure 5 and 200 swept divisions the total element count was 189,200. The solver control settings were also investigated on the base case to identify values that would provide sufficient accuracy in less than 3 hrs. Sufficient accuracy was defined when further tightening of residuals and imbalances delivered a change in the polar phase volume fraction of less than 1%. The identified settings are listed below:

- Time scale – 0.3s (Reduced to 0.01 when using the Turbulent Dispersion force)
- Advection Scheme – High Resolution
- Imbalances – 0.01
- Residuals – 0.0001

Using the above mesh and solver settings, the solution time was approximately three hours on four cores of a dual, quad core cpu (3GHz Xeon) server.

6 Results

Implementing the base case simulation (Table 11) using the aforementioned mesh and solver conditions yielded the simulation results shown in Figure 6. The plots show the polar phase volume fraction dispersed across the face of the reactor tube at different points. The polar phase volume fraction was used as a qualitative simulation result for comparison with the flow visualisation results in Figures 3 and 4. The black lines were used to average the polar phase volume fraction across the line for more accurate comparison when results were not visibly different.

These results clearly indicate that the flow is stratifying where the results in Figure 4 show the flow is highly dispersed. To evaluate the adequacy of the chosen physical models and assess the sensitivity of the model to inputs, parametric studies were performed by changing the following variables independently in the base case (Table 11):

- **Droplet diameter:** 0.04mm to 0.07mm
- **Inlet Velocity:** 0.1m/s to 1m/s
- **Density and Viscosity:** 5 and 10% either side of the base case values
- **Lift Force:** Lift coefficient between 0.1 and 10
- **Virtual Mass Force:** Virtual mass coefficient between 0.1 and 10
- **Wall Lubrication Force:** Tomiyama with pipe diameter = 0.011m
- **Turbulent Dispersion force:** C_{TD} between 0.25 and 1

6.1 Droplet Diameter

The dispersed (polar) phase droplet diameter is a key variable in multi-phase simulations as it determines the interfacial area for momentum, mass and energy transfer and can have a significant effect on simulation results. Table 14 summarises the results of parametric droplet sizes between 0.04 and 0.07mm, while Figure 7 compares the polar phase volume fraction at the outlet of the simulations using the smallest and largest droplet sizes. Both Table 14 and Figure 7 show that stratification increases with increasing droplet size. As the droplet

diameter is increased, both the drag coefficient used by ANSYS CFX and the interfacial area reduce (see Equations 7, 8 and 9), ultimately reducing the drag force. As a result, the net effect of the gravitational force is greater (see Figure 8) causing greater stratification (Figure 7).

6.2 Inlet velocity

In pipe flow, inlet velocity is one of the key variables affecting the level of turbulence. In multi-phase simulations a higher velocity will result in increased turbulence and a higher level of dispersion. The lower velocities ($<0.3 ms^{-1}$) did not converge, as the flow regime in these simulations is no longer dispersed but instead stratified. Figure 9 shows that an increase in velocity reduces the level of stratification, however, even at the unrealistic velocity of 1 m/s the stratification is still present.

6.3 Density and viscosity

To examine the effect of density and viscosity measurement errors, systematic studies were conducted into the density and viscosity of the phases (±5% or 10% on base case) with results shown in Tables 15 and 16, respectively. In these tables the bold type indicates which variables are being altered and the shading is used to clarify the distinction between polar and non-polar phases. It was found that density (Table 15) had a greater effect than viscosity (Table 16) with an 83% change in the bottom polar phase volume fraction (PV bottom) across the non-polar density variations while only a 12% change in the same variable for the changes in viscosity. The effect of density was similar for both phases, that is, a reduction of 10% in the polar phase density (Table 15 row 8) gave similar results to a 10% increase in non-polar phase density (Table 15 row 5). This can be attributed to the buoyancy force which is driven by the density difference between the two phases. The higher the relative density of the polar phase, the greater the stratification and therefore the PV bottom value will be higher.

The influence of density on the level of stratification aligns closely with the experimental observations recorded earlier. Unlike the base case (coconut oil – experiment 2) which had a

density difference of 163.3 kg/m^3 (Table 9) the canola oil feedstock (experiment 1) had a density difference of only 93.4 kg/m^3 (Table 8). This lower density difference, caused by differences in methanol content, resulted in the canola flow visualisation experiment transitioning from stratified to dispersed at a lower velocity than the coconut case (0.26 m/s vs 0.36 m/s).

The viscosity on the other hand had a varied effect depending on the phase in which the viscosity change occurred. As expected, the viscosity of the polar phase droplets had an almost negligible effect on the results as this viscosity does not affect the majority of the flow regime. The effect of the continuous phase viscosity on the flow regime was more significant. The trend, however, was counter-intuitive with a decrease in viscosity increasing stratification. Intuitively a reduction in viscosity represents a reduction in the viscous damping forces of the entire flow thus encouraging turbulence and promoting dispersion. In this case, however, the reduction in viscosity increased stratification. This can be understood by considering the effect of continuous phase viscosity on the drag coefficient. Examination of Equation 12 shows that a reduction in the continuous phase viscosity decreases the mixture viscosity, which increases the particle Reynolds number and thus decreases the drag coefficient which as discussed in the section on droplet diameter encourages stratification. The lesser effect of the viscosity in comparison with density is due to the greater magnitude of the buoyancy force than the drag force.

6.4 Lift, virtual mass and wall lubrication force

The parametric studies conducted on the base case varying the lift, virtual mass and wall lubrication force had a negligible effect on the polar phase distribution unless the coefficient was increased to levels that were physically impossible. The limited effect of these interphase forces observed in this study harmonises with the work of Hussain (2004). The reasons for the limited effect of these forces are due to the physical nature of this system. Both the slip velocity and relative phasic accelerations are low and consequently both the lift force and virtual mass force are negligible. Furthermore, the wall lubrication force is more applicable to larger diameter bubbles than small diameter droplets.

6.5 Turbulent dispersion force

Inclusion of the turbulent dispersion force is particularly relevant for this simulation as it models the dispersion of particles/droplets caused by the turbulence induced eddies present in the continuous phase (Burns *et al.*, 2004). Hussain (2004) reported that the turbulent dispersion force had a strong effect on the simulation results, however, stratification was still slowly occurring. The turbulent dispersion force strongly depends on the velocity gradients present in the flow regime which can easily be lost with a mesh that is too coarse. Examination of the mesh used in Hussain's study suggests that it was too coarse, especially in the boundary layer. This lack of resolution is mainly the result of limited computational resources available 10 years ago.

The greater computational resources available in this study made it possible to further investigate the effect of the turbulent dispersion force. Initial investigations into this force were unproductive with both the Lopez de Bertanado and Favre averaged force failing to converge and simply oscillating at relatively high residual values. This was rectified by reducing the physical time-step to 0.01s and gradually increasing the turbulent dispersion coefficient in the Lopez de Bertodano force using the following CEL (CFX Expression Language) expression:

$$\min(0.5,0.01*\text{aitrn})$$

Equation 17: Gradual increase of turbulent dispersion coefficient

This ensured that the turbulent dispersion coefficient would build up to the desired value (0.5) in 0.01 increments per iteration while maintaining stability (aitrn is the CEL variable name of the iteration number). In Equation 17, the 0.5 represents the actual coefficient used in the simulation, as after 50 iterations 0.5 is the constant output. The choice of time-step was based on a systematic process of reducing time step by a factor of 10 until there a converged and time scale independent solution was achieved. The smaller timescale increases the stability of the solution and prevents oscillation.

Results of these simulations for experiment one are shown in Figures 10 and 11 and results for experiment two are shown in Figures 12 and 13. These figures provide plots of the polar phase volume fraction at the end of the 4m tube in the simulation. At low velocities in both cases there is clear evidence of stratification with a concentration of the polar phase at the bottom and an absence at the top of the tube. At higher velocities the polar phase volume fraction across the face is more uniform with only the slightest amount of stratification present which can be seen in the corresponding visualisation results.

At the time of writing the CFX 12 solver was unstable when the favre averaged model was implemented (even with the incremental increase of C_{TD}), however, it is expected that more current versions of the CFX solver will be able to solve this allowing the model to be more widely applicable to different reactor geometries.

The comparison of simulation results with experimental results shown in the above figures confirms the suitability of this CFD model for the prediction of flow dispersion/stratification in tubular methanolysis reactors. To be conservative a Turbulent Dispersion coefficient of 0.3 should be used in the model to determine whether a particular flow conditions is stratified or dispersed. Although, this model has not been quantitatively validated, there is enough qualitative evidence to suggest the model is suitable for determining the flow pattern at a particular set of conditions.

7 Conclusion

The alignment of the simulation with the corresponding flow visualisation results in Figures 3 and 4 demonstrates that it is possible to qualitatively model the distribution of the polar phase in the non- polar phase through the inclusion of the drag force and turbulent dispersion force in the multi-phase model. This achievement advances the application of CFD modeling in liquid-liquid flows in three ways. Firstly, this model provides a method for predicting the flow regime of two phase reactions in the production of biodiesel while also laying a foundation for a comprehensive two phase model of the reaction. Secondly, it provides key information (phase data and model parameters) for CFD models of other biodiesel reactors

(e.g.: Jet reactors, ultrasonic reactors and oscillatory flow reactors). Finally, the alignment of model outputs with real world data demonstrates that by inclusion of the turbulent dispersion force it is possible to accurately model any liquid-liquid flow in tubular reactors or pipes.

This fundamental research will provide other researchers and technology developers with starting points for CFD models of more complicated biodiesel reactor geometries and other liquid-liquid flows.

Acknowledgements

The authors would like to acknowledge: Australian Government, Murdoch University, Centre for Research into Energy for Sustainable Transport (CREST) and Bluediesel for their funding support and provision of infrastructure; LEAP Australia for the provision of ANSYS CFX; The Australian Lubricant Manufacturing Company (ALMC) for the use of their equipment and Allira glass blowing for assistance in the experimental design.

Nomenclature

Variables:

Re	Reynolds
D	Pipe diameter (m)
d	Pipe diameter (m)
ρ	Density (kg/m^3)
μ	Viscosity (Pa s)
U	Superficial velocity (m/s)
U	Velocity vector (m/s)
r	Volume fraction
m	Correlation coefficient
n	Correlation coefficient
T	Temperature (°C)
F	Force
A	Area
M	Lopez De Bertodano force
C	Coefficient (dependent on subscripts)

Sub/super script:

i	Either phase

α	Phase A
β	Phase B
c	Continuous phase
d	Dispersed phase
m	Mixture
p	Pipe
L	Lift force
VM	Virtual Mass Force

8 References

Abraham, J. P., Sparrow, E. M., & Tong, J. C. K. (2008). Breakdown of Laminar Pipe Flow into Transitional Intermittency and Subsequent Attainment of Fully Developed Intermittent or Turbulent Flow. *Numerical Heat Transfer, Part B: Fundamentals: An International Journal of Computation and Methodology, 54*(2), 103-115.

Adeyemi, N., Mohiuddin, A. K. M., & Nor, M. I. M. (2013). CFD Modelling of Waste Cooking Oil Transesterification in a Stirred Tank Reactor. *World Applied Sciences Journal 21 (Mathematical Applications in Engineering)*, 151-158.

Akoh, C. C., Chang, S.-W., Lee, G.-C., & Shaw, J.-F. (2007). Enzymatic Approach to Biodiesel Production. *Journal of Agricultural and Food Chemistry, 55*(22), 8995-9005.

Al-Wahaibi, T., & Angeli, P. (2007). Transition between stratified and non-stratified horizontal oil-water flows. Part I: Stability analysis. *Chemical Engineering Science, 62*(11), 2915-2928.

Al-Wahaibi, T., Smith, M., & Angeli, P. (2007). Transition between stratified and non-stratified horizontal oil-water flows. Part II: Mechanism of drop formation. *Chemical Engineering Science, 62*(11), 2929-2940.

Allen, C. A. W. (1999). Predicting the viscosity of biodiesel fuels from their fatty acid ester composition. *Fuel, 78*, 1319-1326.

ANSYS. (2009). *ANSYS CFX-Solver Theory Guide*. User Manual.

Boocock, D. G. B., Konar, S. K., Mao, V., Lee, C., & Buligan, S. (1998). Fast formation of high-purity methyl esters from vegetable oils. *J. Am. Oil Chem. Soc., 75*(9), 1167-1172.

Boocock, D. G. B., Konar, S. K., Mao, V., & Sidi, H. (1996). Fast one phase oil-rich process for the preparation of vegetable oil methyl esters. *Biomass and bioenergy, 11*(1), 43-50.

Burns, A. D., Frank, T., Hamill, I., & Shi, J.-M. (2004, may 30 - June 4). *The Favre Averaged Drag Model for Turbulent Dispersion in Eulerian Multi-Phase Flows.* Paper presented at the 5th International Conference on Multiphase Flow, Yokohama, Japan.

Coupland, J. N., & McClements, D. J. (1997). Physical Properties of Liquid Edible Oils. *JAOCS, 74*(12), 1559-1564.

Darnoko, D., & Cheryan, M. (2000). Kinetics of palm oil transesterification in a batch reactor. *JAOCS, 77*(12), 1263-1267.

de Boer, K. (2010). *Optimised Small Scale Reactor Technology, a new approach for the Australian Biodiesel Industry.* (PhD Thesis), School of Engineering and Energy, Murdoch University, Perth, Western Australia.

de Boer, K., & Bahri, P. A. (2009). *Investigation of Liquid-Liquid two phase flow in biodiesel production*. Paper presented at the Seventh International Conference on CFD in the Minerals and Process Industries CSIRO, Melbourne.

de Boer, K., & Bahri, P. A. (2011). Supercritical methanol for fatty acid methyl ester production: A review. *Biomass & Bioenergy, 35*(3), 983-991. doi: 10.1016/j.biombioe.2010.11.037

Doell, R., Konar, S. K., & Boocock, D. G. B. (2008). Kinetic parameters of homogeneous transmethylation of soybean oil. *J. Am. Oil Chem. Soc., 85*, 271-276.

Freedman, B., Butterfield, R. O., & Pryde, E. H. (1986). Transesterification kinetics of soybean oil. *J. Am. Oil Chem. Soc., 63*(10), 1375-1380.

Hussain, S. A. (2004). *Experimental and Computational Studies of Liquid-Liquid Dispersed Flows.* (PhD Thesis), Univeristy of London, London.

Karmee, S. k., Chandna, D., Ravi, R., & Chadha, A. (2006). Kinetics of base catalyzed transesterification of triglycerides from pongamia oil. *J. Am. Oil Chem. Soc., 83*(10), 873-877.

Kimmel, T. (2004). *Kinetic Investigation of the base-catalysed glycerolysis of Fatty Acid Methyl Esters* (PhD Thesis), Technical University of Berlin, Berlin.

Krisnangkura, K., Yimsuwan, T., & Pairintra, R. (2006). An emperical approach in predicting biodiesel viscosity at various temperatures. *Fuel, 85*, 107-113.

Liew, K. Y., Seng, C. E., & Oh, L. L. (1992). Viscosities and Densities of the Methyl esters of some n-Alkanoic Acids. *J. Am. Oil Chem. Soc., 69*(2).

Lotero, E., Goodwin, J. G., Bruce, D. A., Suwannakarn, K., Liu, Y., & Lopez, D. E. (2006). The catalysis of Biodiesel synthesis. *Catalysis, 19*, 41-83.

Ma, F., Clements, D., & Hanna, M. (1999). The effect of mixing on transesterification of beef tallow. *Bioresource Technology, 69*, 289-293.

Mittelbach, M., & Remschmidt, C. (2006). *Biodiesel the comprehensive handbook*. Vienna: Martin Mittelbach.

Negi, D. S. (2006). *Base Catalyzed Glycerolysis of Fatty Acid Methyl Esters: Investigations Toward the Development of a Continuous Process.* (PhD Thesis), Technical University of Berlin, Berlin.

Negi, D. S., Sobotka, F., Kimmel, T., Wozny, G., & Schomacker, R. (2006). Liquid-Liquid Phase Equilibrium in Glycerol-Methanol-Methyl Oleate and Glycerol-Monoolein - Methyl oleate ternary systems. *Ind. Eng. Chem. Res., 45*, 3693-3696.

Noureddini, H., & Zhu, D. (1997). Kinetics of Transesterification of soybean oil. *J. Am. Oil Chem. Soc., 74*(11), 1457-1463.

Orifici, L. I., Bahl, C. D., Gely, M. C., Bandoni, A., & Pagano, A. M. (2013). Modeling and Simulattion of the biodiesel production in a pilot continuous reactor. *Mecanica Computacional, XXXII*, 1451-1461.

Ranade, V. V. (2002). *Computational Flow Modelling for Chemical Reactor Engineering* (Vol. 5). London: Academic Press.

Sheehan, J., Camobreco, V., Duffield, J., Graboski, M., & Shapouri, H. (1998). *Life Cycle inventory of biodiesel and petroleum diesel for use in an urban bus*. (NREL/SR-580-24089). National Renewable energy Laboratory Retrieved from http://www.nrel.gov/docs/legosti/fy98/24089.pdf.

Spriggs, H. D. (1973). Comments on Transition from Laminar to Turbulent Flow. *Industrial & Engineering Chemistry Fundamentals, 12*(3), 286-290. doi: doi:10.1021/i160047a004

Stamenkovic, O. S., Lazic, M. L., Todorovic, Z. B., Veljkovic, V. B., & Skala, D. U. (2007). The effect of agitation intensity on alkali-catalyzed methanolysis of sunflower oil. *Bioresource Technology, 98*, 2688-2699.

Stamenkovic, O. S., Todorovic, Z. B., Lazic, M. L., Veljkovic, V. B., & Skala, D. U. (2008). Kinetics of sunflower oil methanolysis at low temperatures. *Bioresource Technology, 99*, 1131-1140.

Stanbridge, D., & Sullivan, J. (1999). *One example of how offshore oil and industry technology can be of benefit to hydrometallurgy*. Paper presented at the Second international conference on CFD in the minerals and process industries (CSIRO), Melbourne, Australia.

Versteeg, H. K., & Malalsekera, W. (2007). *An Introduction to Computational Fluid Dynamics* (2nd ed.). Harlow: Pearson.

Vicente, G., Martinez, M., & Aracil, J. (2003). Integrated Biodiesel production: A comparison of different homogeneous catalyst systems. *Bioresource Technology, 92*, 297-305.

Vicente, G., Martinez, M., & Aracil, J. (2005a). Optimization of Brassica carinata oil methanolysis for biodiesel production. *J. Am. Oil Chem. Soc., 82*(12), 899-904.

Vicente, G., Martinez, M., Aracil, J., & Esteban, A. (2005b). Kinetics of Sunflower Oil Methanolysis. *Ind. Eng. Chem. Res., 44*, 5447-5454.

Wang, W.-C., Natelson, R. H., Stikeleather, L. F., & Roberts, W. L. (2012). CFD Simulation of transient stage of continuous countercurrent hydrolysis of canola oil. *Computers and chemical engineering, 43*, 108-119.

Wulandani, D., Ilham, F., Hagiwara, S., & Nabetani, H. (2012). The effect of obstacle types on the behavior of methanol bubble in the triglyceride within the column reactor by using CFD simulation. *Journal of Mechanical Engineering and Technology, 4*(2), 61-68.

Zhou, W., & Boocock, D. G. B. (2006). Phase behavior of the base catalyzed transesterification of soybean oil. *J. Am. Oil Chem. Soc., 83*(12), 1041-1045.

Development and Validation of a two phase CFD model for tubular Biodiesel Reactors

Karne de Boer[2] and Parisa A. Bahri

School of Engineering and Information Technology, Murdoch University, Perth, Western Australia

1 Figures

Please see the correspondingly named tiff files submitted with this article

Figure 1: Sigmoidal reaction progression

Figure 2: Flow Visualisation Equipment

Figure 3: Experiment one visualisation results

Figure 4: Experiment two visualisation results

Figure 5: Chosen face mesh

Figure 6: Base case simulation results – developing flow profile

Figure 7: Comparison of droplet size simulation results

Figure 8: Forces acting on a falling polar phase droplet

Figure 9: Comparison of results for velocity parametric studies

Figure 10: Simulation results for Canola at velocities 0.243-0.32m/s with a TD of 0.4

Figure 11: Simulation results for Canola at velocities 0.2-0.229m/s with a TD of 0.4

Figure 12: Simulation results for Coconut at velocities 0.358 – 0.315m/s with a TD of 0.5

Figure 13: Simulation results for Coconut at velocities 0.258 – 0.301m/s with a TD of 0. 5

2 Tables

Table 1: Summary of experimental conditions

[2] Corresponding author Email: karne@regenerateindustries.com

Experiment Number	Description	Transition Speed	Variables
One	Raw canola oil (Aus-oils Kojonup, Western Australia) used as feedstock with flow velocity gradually increased from 0.186m/s to 0.320m/s	18-19 Hz	**Methanol Ratio:** ~6:1 **Catalyst:** ~0.75% **Reactor in Temp:** 118˚C **Reactor Out Temp:** 84˚C **Midpoint Temp:** 101°C
Two	Refined Bleached and Dried coconut oil used as feedstock, with flow velocity gradually increased from 0.143 to 0.358m/s	25 Hz	**Methanol Ratio:** 5:1 **Catalyst:** 0.5% **Reactor in Temp:**115˚C **Reactor Out Temp:** 67˚C **Midpoint Temp:** 91°C

Table 2: Experiment one (canola) viscosity and density data for non-polar phase

Temperature	Dynamic Viscosity	Density
°C	*mPa.s*	*g/cm3*
30	3.8195	0.8671
33	3.5641	0.8647
36	3.3342	0.8624
39	3.1368	0.8601
42	2.9366	0.8579
45	2.7641	0.8557
48	2.6065	0.8534
52	2.416	0.8503
55	2.2862	0.8479
58	2.1673	0.8457

61	2.0565	0.8435
64	1.9412	0.8416
67	1.8445	0.8386

Table 3: Experiment one (canola) viscosity and density data for polar phase

Temp	**Dynamic Viscosity**	**Density**
°C	*mPa.s*	*g/cm3*
30	3.5843	0.9584
33	3.2913	0.9558
36	3.013	0.9533
39	2.8016	0.951
42	2.5968	0.9484
45	2.4132	0.9461
48	2.2452	0.9436
51	2.0945	0.941
54	1.9585	0.9385
57	1.8342	0.936
60	1.7223	0.9336
63	1.6189	0.9309

Table 4: Experiment two (coconut) viscosity and density data for non-polar phase

Temp	**Dynamic Viscosity**	**Density**
°C	*mPa.s*	g/cm^3
30	3.2313	0.8678
35	2.9663	0.8638
40	2.6661	0.8599

45	2.4078	0.856
50	2.1817	0.8518
55	2.008	0.848
60	1.8295	0.8437
65	1.6526	0.84
70	1.535	0.8359

Table 5: Experiment two (coconut) viscosity and density data for polar phase

Temp	**Dynamic Viscosity**	**Density**
°C	*mPa.s*	*g/cm3*
30	14.607	1.0317
33	12.982	1.0296
36	11.61	1.0275
39	10.396	1.0253
42	9.3513	1.0231
45	8.4424	1.0209
48	7.6347	1.0187
51	6.923	1.0164
54	6.2985	1.0137
57	5.77291	1.0114
60	5.2398	1.0091
63	4.7953	1.0068
66	4.409	1.045
69	4.0069	1.0022
72	3.7285	0.9998

Table 6: Density correlations of different phases

Phase	ρ_0	ρ_1	R^2
Canola FAME	889.8	-0.8	0.9997
Canola Glycerol	983.2	-0.8	0.9999
Coconut FAME	891.8	-0.8	0.9999
Coconut Glycerol	1055.1	-0.8	0.9996

Table 7: Viscosity correlations of different phases and mixtures

Phase	m	n	T_0	SSE
Canola FAME	-1.661	508.4	76.43	0.000244
Canola Glycerol	-1.570	362.4	132.5	0.000372
Coconut FAME	-2.133	750.0	19.85	0.00281
Coconut Glycerol	-2.462	778.5	88.39	0.00648

Table 8: Fluid properties for experiment one

Phase	Density (kg/m^3)	Viscosity (cP)
Polar	902.4	0.851
Non-polar	809.0	1.113

Table 9: Fluid properties for experiment two

Phase	Density (kg/m^3)	Viscosity (cP)
Polar	982.3	2.297
Non-polar	819	1.110

Table 10: Reynolds Number

Superficial Velocity	Reynolds Number
Canola (Figure 3)	
0.215 m/s (Stratified)	1812

0.243 m/s (Transition)	2048
0.272 m/s (Dispersed)	2293
Coconut (Figure 4)	
0.172 m/s (Stratified)	1239
0.272 m/s (Transition)	1959
0.358m/s (Dispersed)	2579

Table 11: Simulation Settings

Variable/Setting	**Typical Value**
Dispersed droplet diameter	0.055mm
Fluid Physical Properties	Tables 9 (Experiment 2 - Coconut)
Free surface model	None
Homogeneity	Inhomogeneous
Turbulence **(Fluid dependent)**	*Continuous:* k-Epsilon *Dispersed:* Dispersed phase zero equation
Surface tension coefficient	0.0292 J/m2
Drag Force	Ishii-Zuber

Table 12: Boundary Conditions

Boundary	**Value**
Inlet (Normal speed)	$0.358ms^{-1}$
Outlet (Average Static Pressure)	20psi
Tube wall	Smooth, no-slip wall

Table 13: Mesh parameters

Parameter	Setting
Face Sizing	0.0003m
Edge Sizing	80 divisions (hard)
Inflation	20 layers, Max thickness of 3mm and expansion of 1.1

Table 14: Parametric droplet size studies

Droplet Size (mm)	PPV Top	PPV Middle	PPV Bottom
0.04	0.1454	0.1500	0.2494
0.05	0.0198	0.1500	0.4984
0.055	0.0021	0.1499	0.5961
0.06	0.0002	0.1499	0.6551
0.07	0.0000	0.1499	0.7019

Table 15: Parametric study results for non polar phase and polar phase density

Row #	Non Polar Density (kgm^{-3})	Polar Density (kgm^{-3})	Non Polar Viscosity (Cp)	Polar Viscosity (Cp)	PPV Bottom	PPV Middle	PPV Top
1	819	982.3	1.11	2.297	0.5961	0.1500	0.0021
2	**778**	982.3	1.11	2.297	0.6636	0.1500	0.0003
3	**860**	982.3	1.11	2.297	0.4206	0.1499	0.0474
4	**737**	982.3	1.11	2.297	0.6885	0.1500	0.0001
5	**901**	982.3	1.11	2.297	0.1955	0.1499	0.1492
6	819	**1031.1**	1.11	2.297	0.6677	0.1499	0.0001
7	819	**932.9**	1.11	2.297	0.3774	0.1500	0.0738
8	819	**883.8**	1.11	2.297	0.1763	0.1500	0.1519
9	819	**1080.2**	1.11	2.297	0.6919	0.1499	0.0000

Table 16: Parametric study results for non polar phase and polar phase viscosity

Row #	Non Polar Density (kgm^{-3})	Polar Density (kgm^{-3})	Non Polar Viscosity (Cp)	Polar Viscosity (Cp)	PPV Bottom	PPV Middle	PPV Top
1	819	982.3	1.11	2.297	0.5961	0.1500	0.0021
2	819	982.3	**1.16**	2.297	0.5783	0.1500	0.0038
3	819	982.3	**1.05**	2.297	0.6147	0.1499	0.0010
4	819	982.3	**0.99**	2.297	0.6299	0.1499	0.0004
5	819	982.3	**1.22**	2.297	0.5587	0.1500	0.0072
6	819	982.3	1.11	**2.412**	0.5961	0.1499	0.0023
7	819	982.3	1.11	**2.18**	0.5987	0.1500	0.0020
8	819	982.3	1.11	**2.07**	0.5985	0.1500	0.0019
9	819	982.3	1.11	**2.53**	0.5961	0.1499	0.0024

Figure(s)

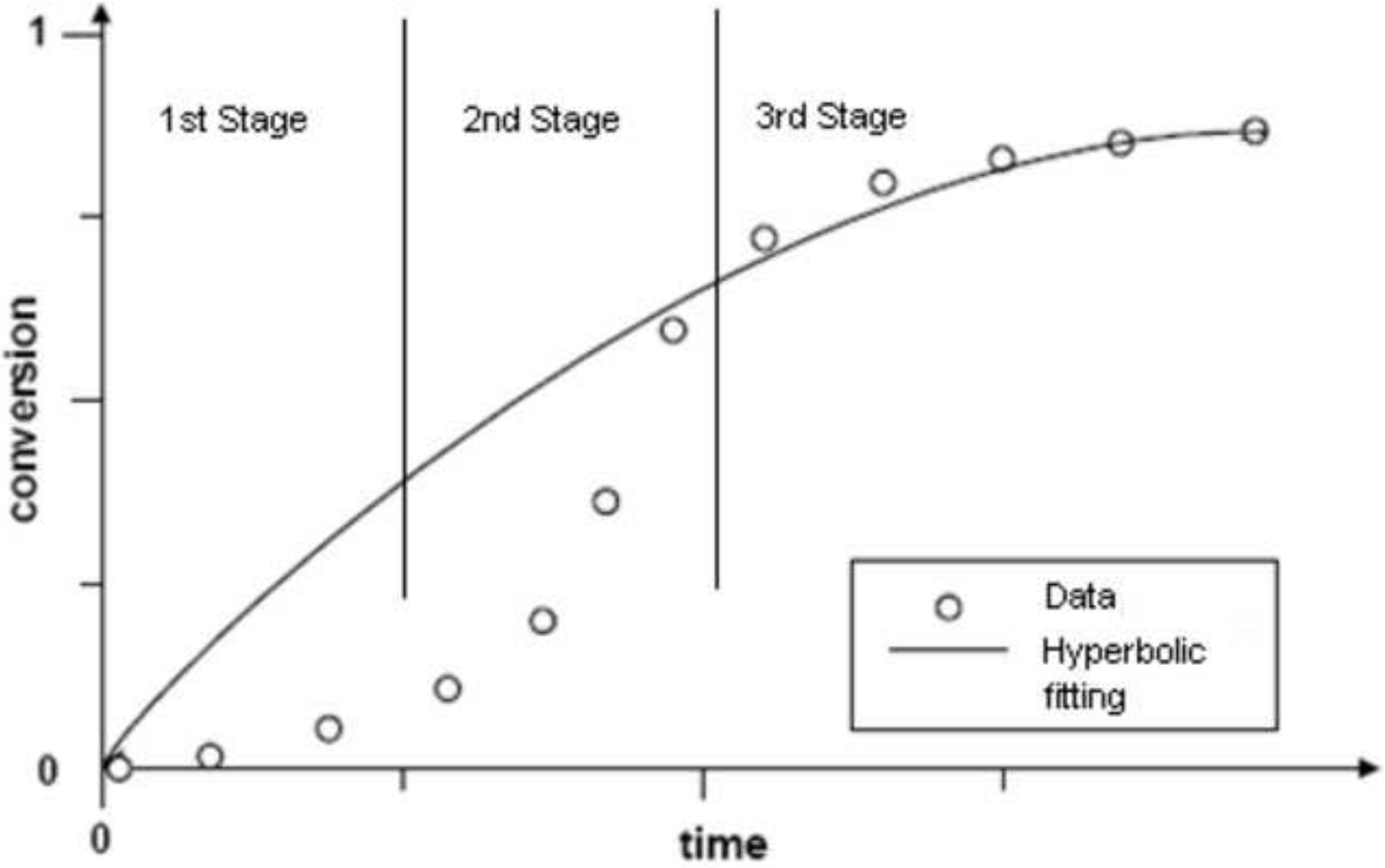
1
0
0
conversion
time
1st Stage
2nd Stage
3rd Stage
Data
Hyperbolic fitting

Figure(s)

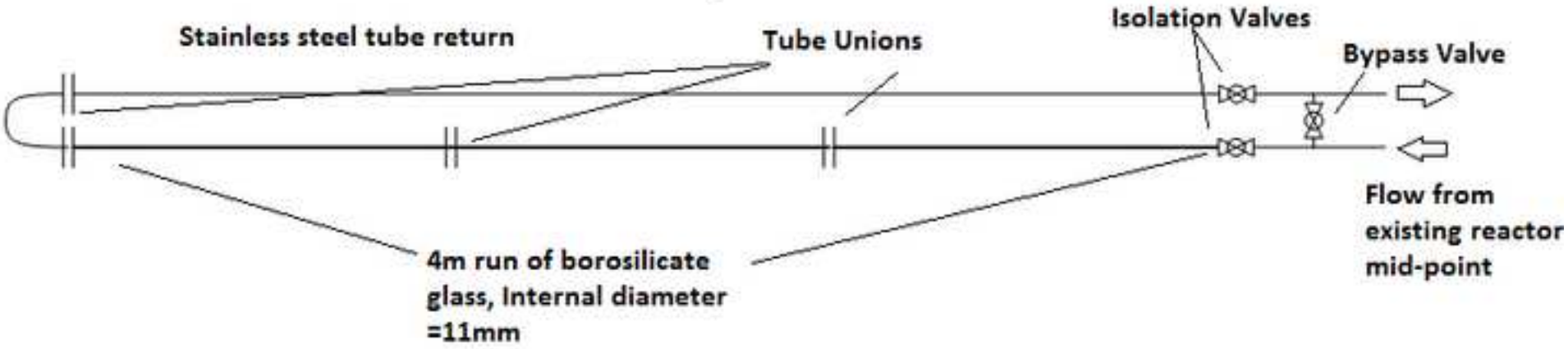
Stainless steel tube return
Tube Unions
Isolation Valves
Bypass Valve
Flow from existing reactor mid-point
4m run of borosilicate glass, Internal diameter =11mm

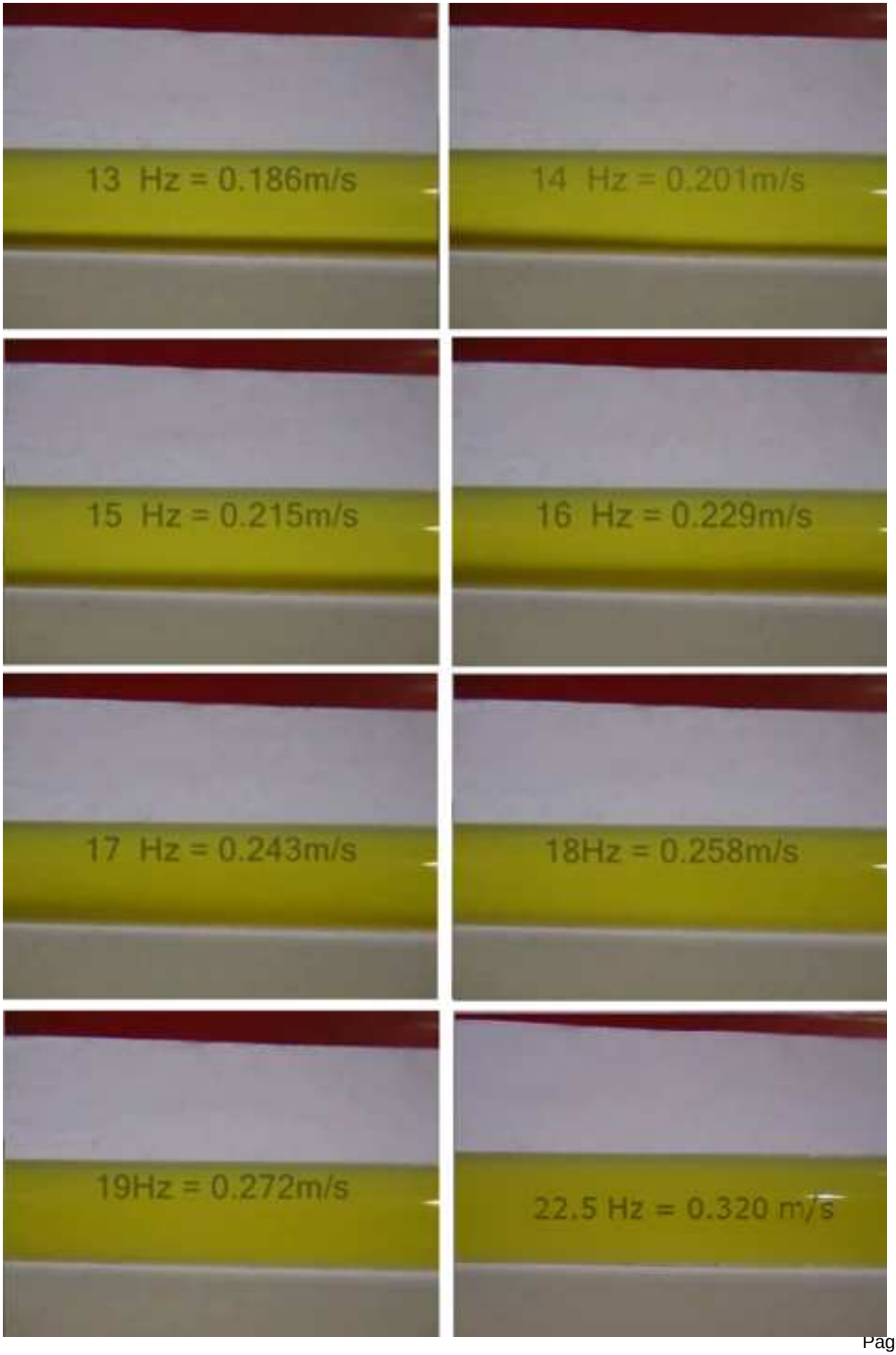

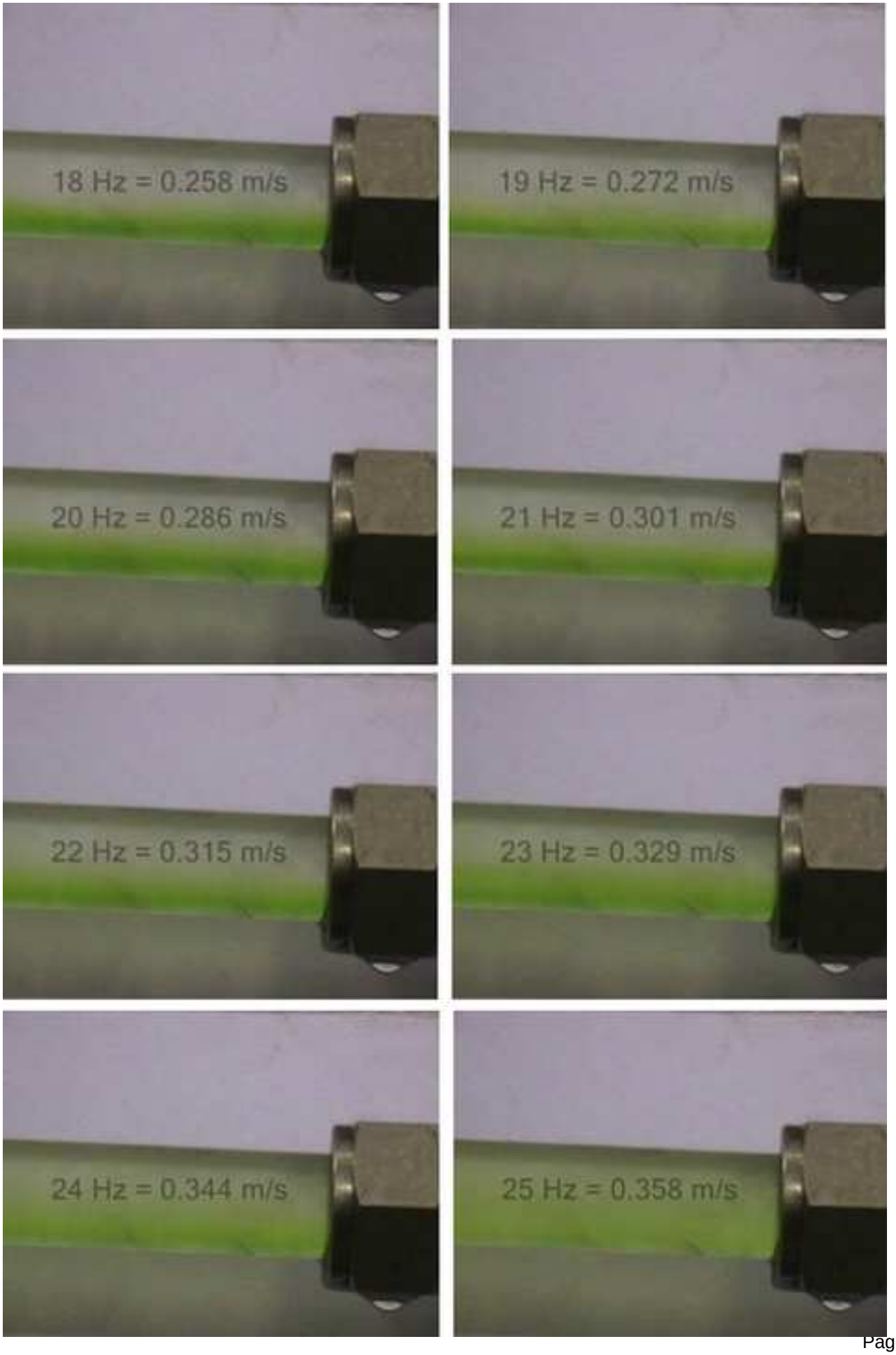

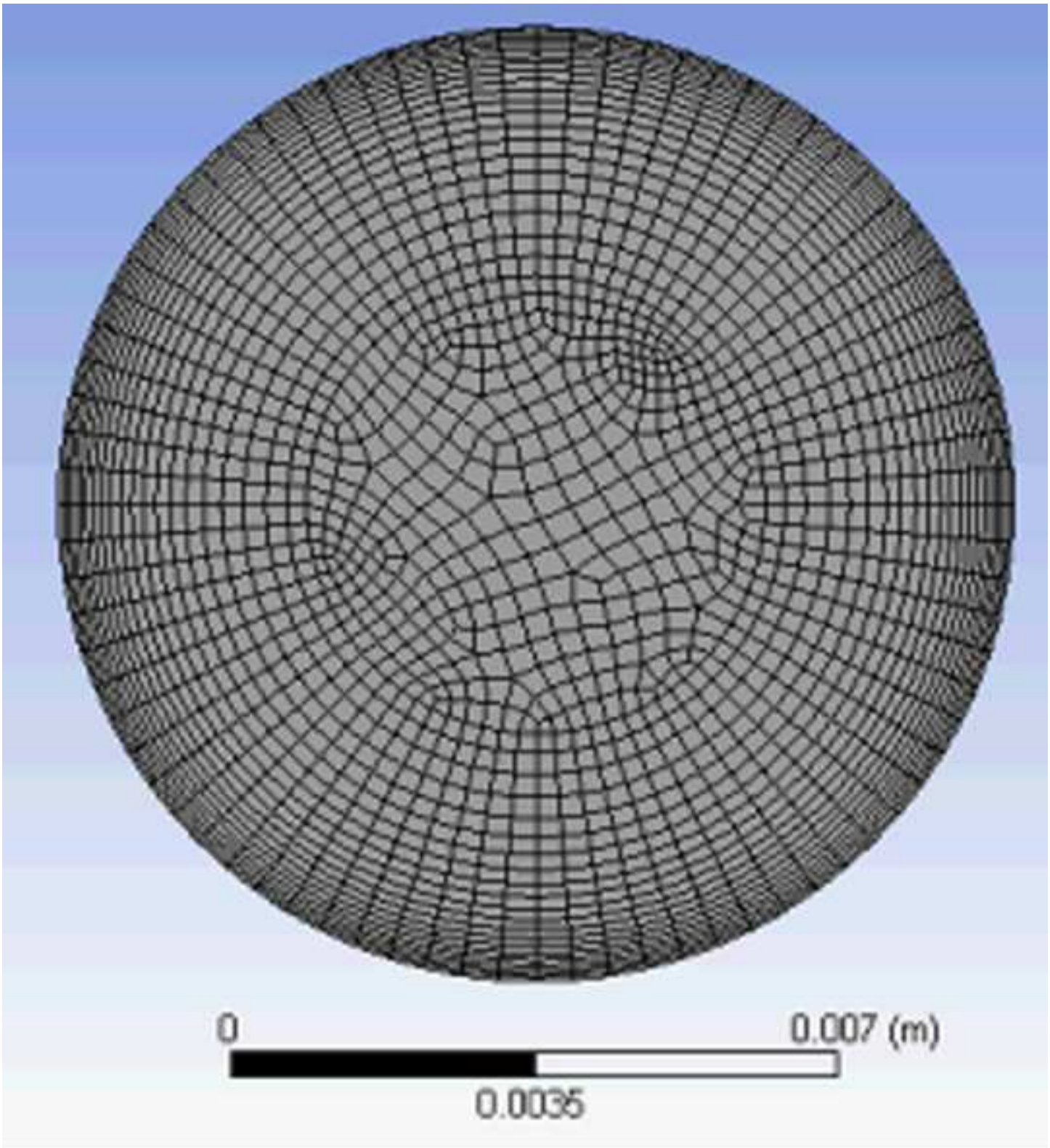

Figure(s)

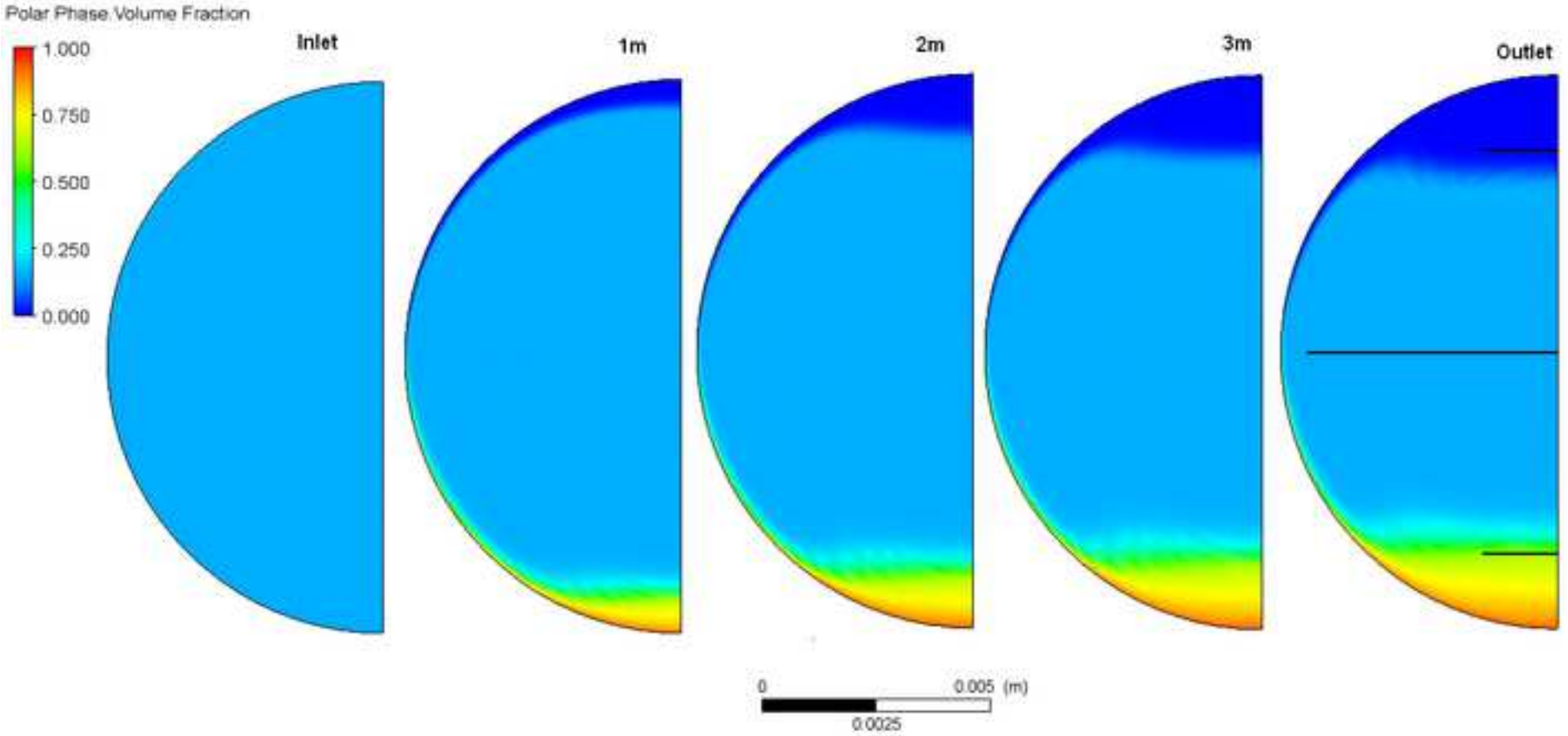
Polar Phase Volume Fraction
1.000
0.750
0.500
0.250
0.000
Inlet
1m
2m
3m
Outlet
0
0.005 (m)
0.0025

Figure(s)

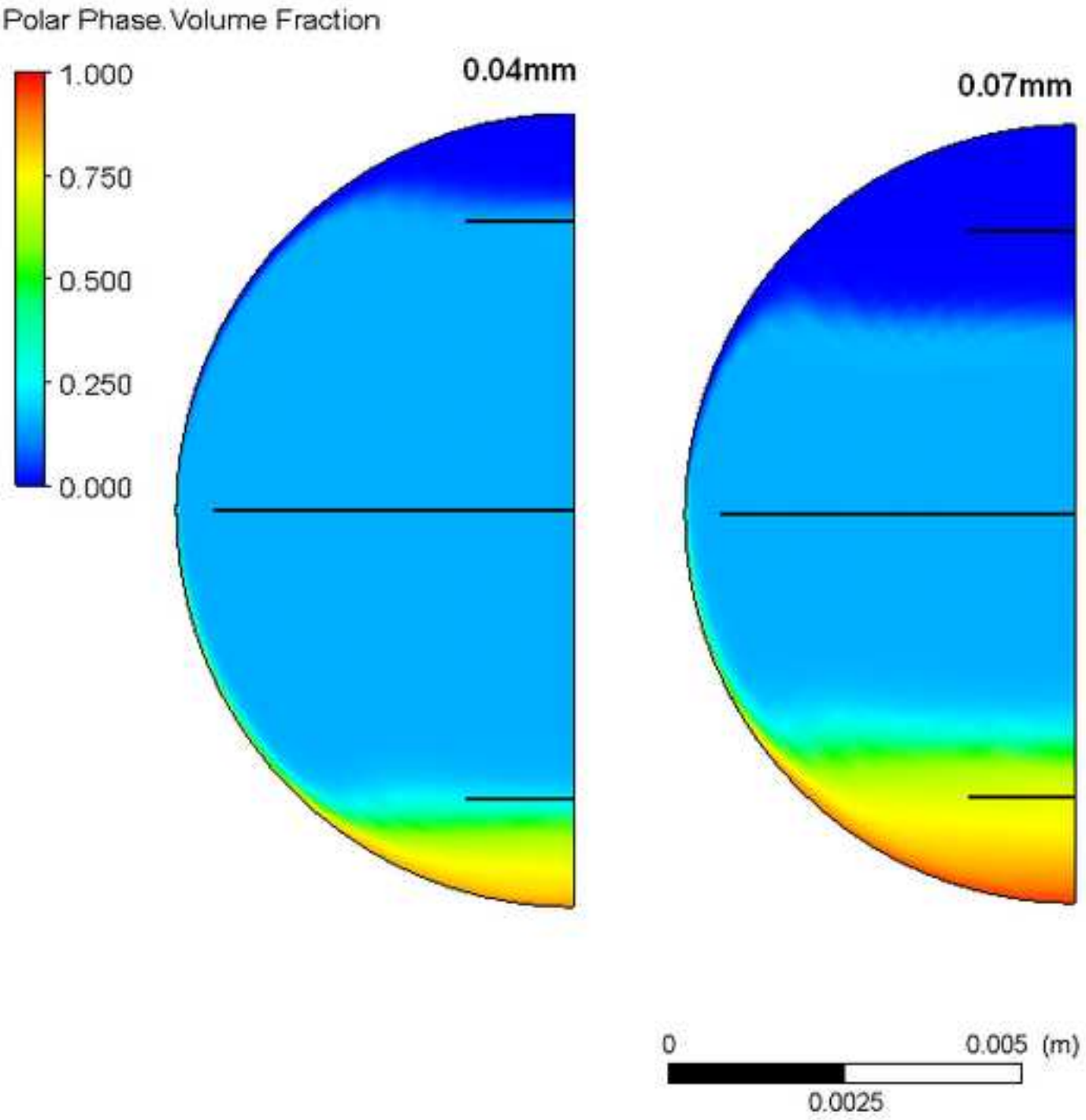
Polar Phase.Volume Fraction
1.000
0.750
0.500
0.250
0.000
0.04mm
0.07mm
0
0.005 (m)
0.0025

Figure(s)

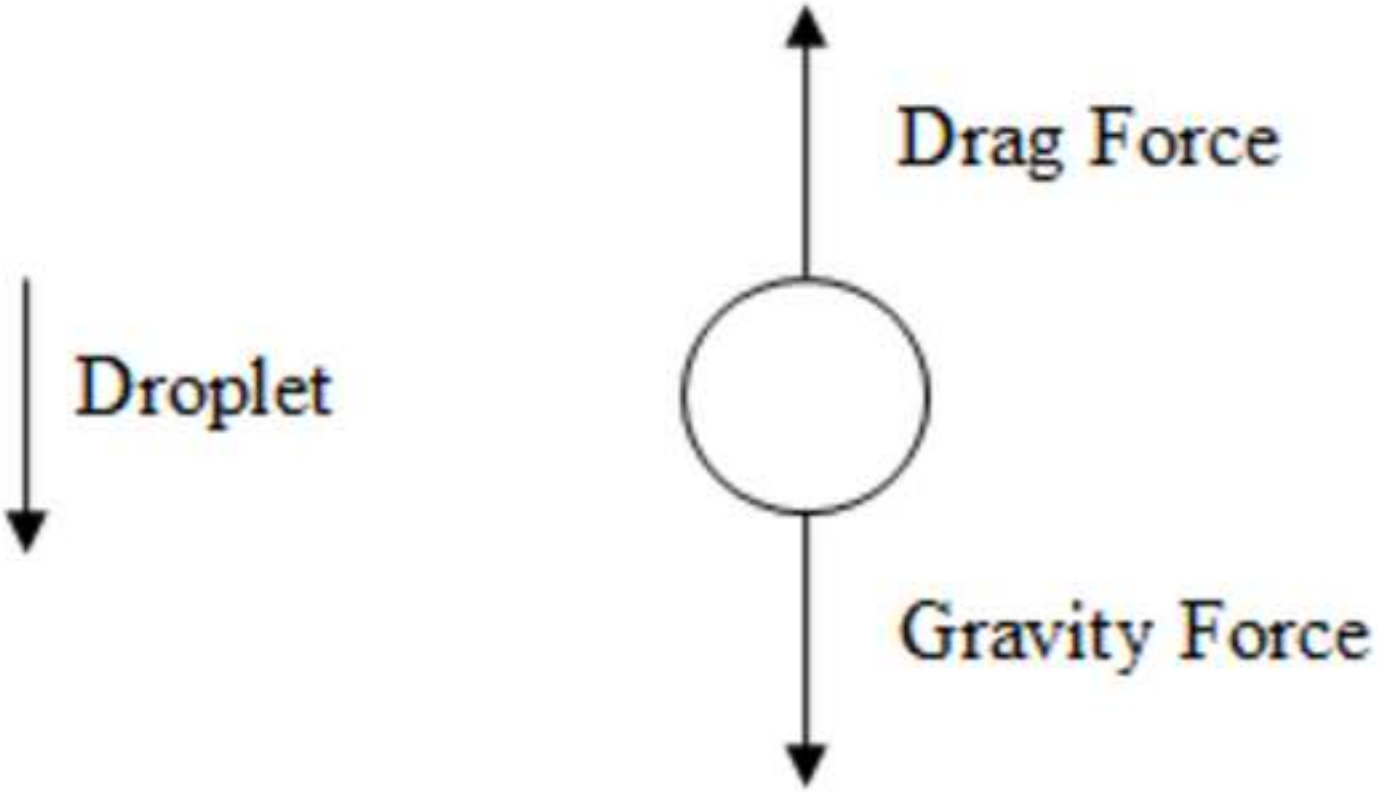

Figure(s)

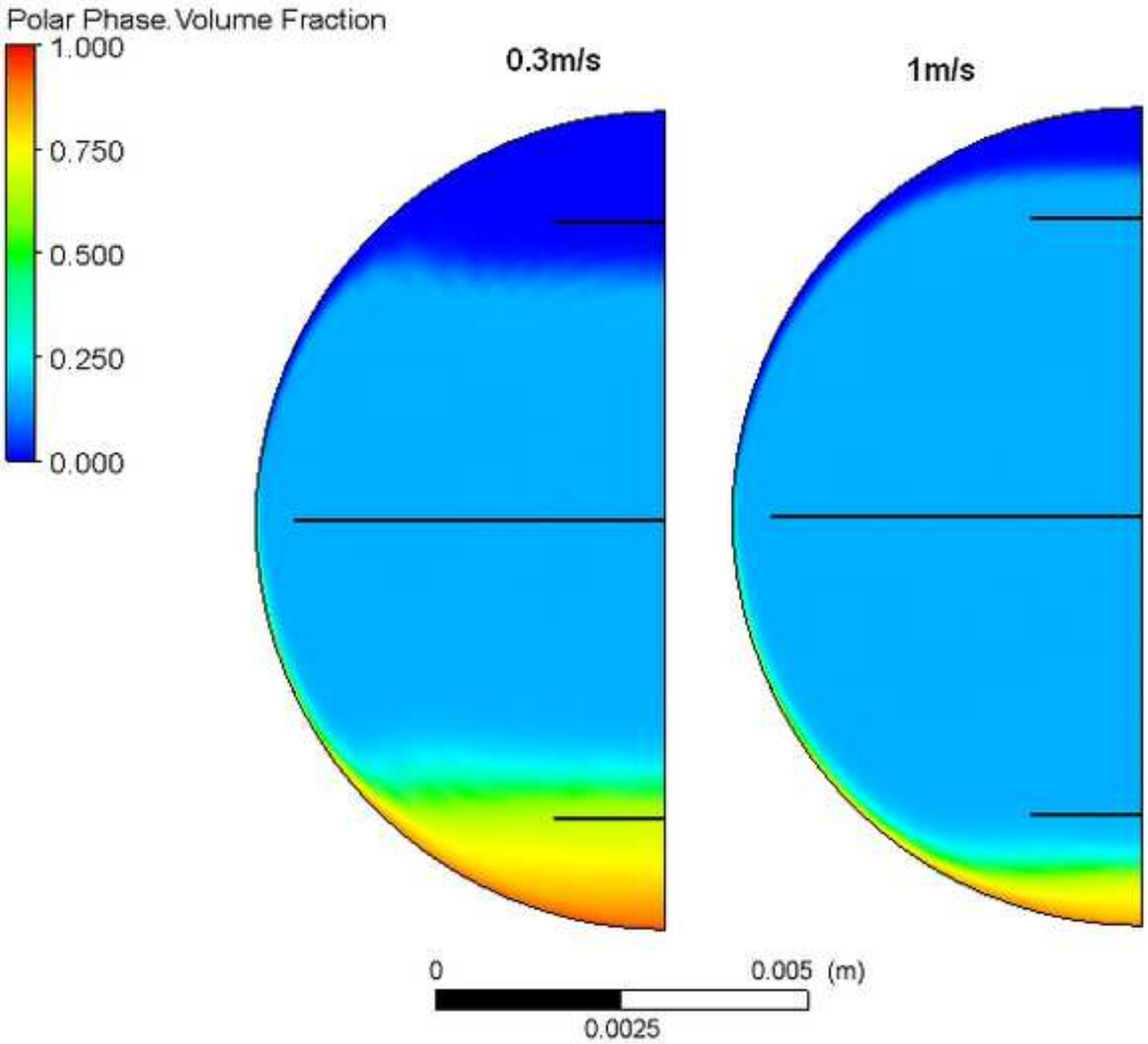
Polar Phase.Volume Fraction
1.000
0.750
0.500
0.250
0.000
0.3m/s
1m/s
0
0.005 (m)
0.0025

Figure(s)

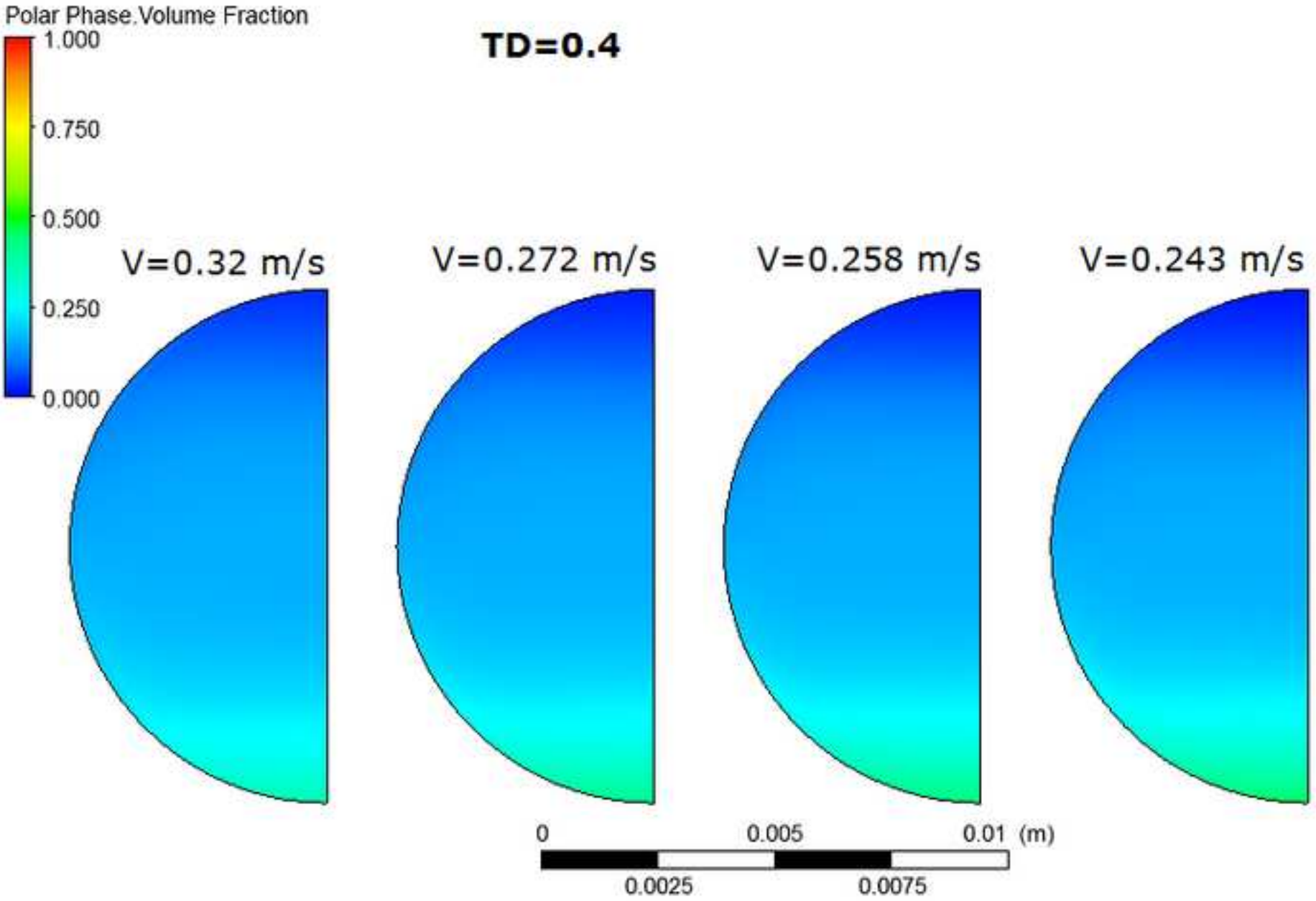
Polar Phase.Volume Fraction
1.000
0.750
0.500
0.250
0.000
TD=0.4
V=0.32 m/s
V=0.272 m/s
V=0.258 m/s
V=0.243 m/s
0
0.005
0.01 (m)
0.0025
0.0075

Figure(s)

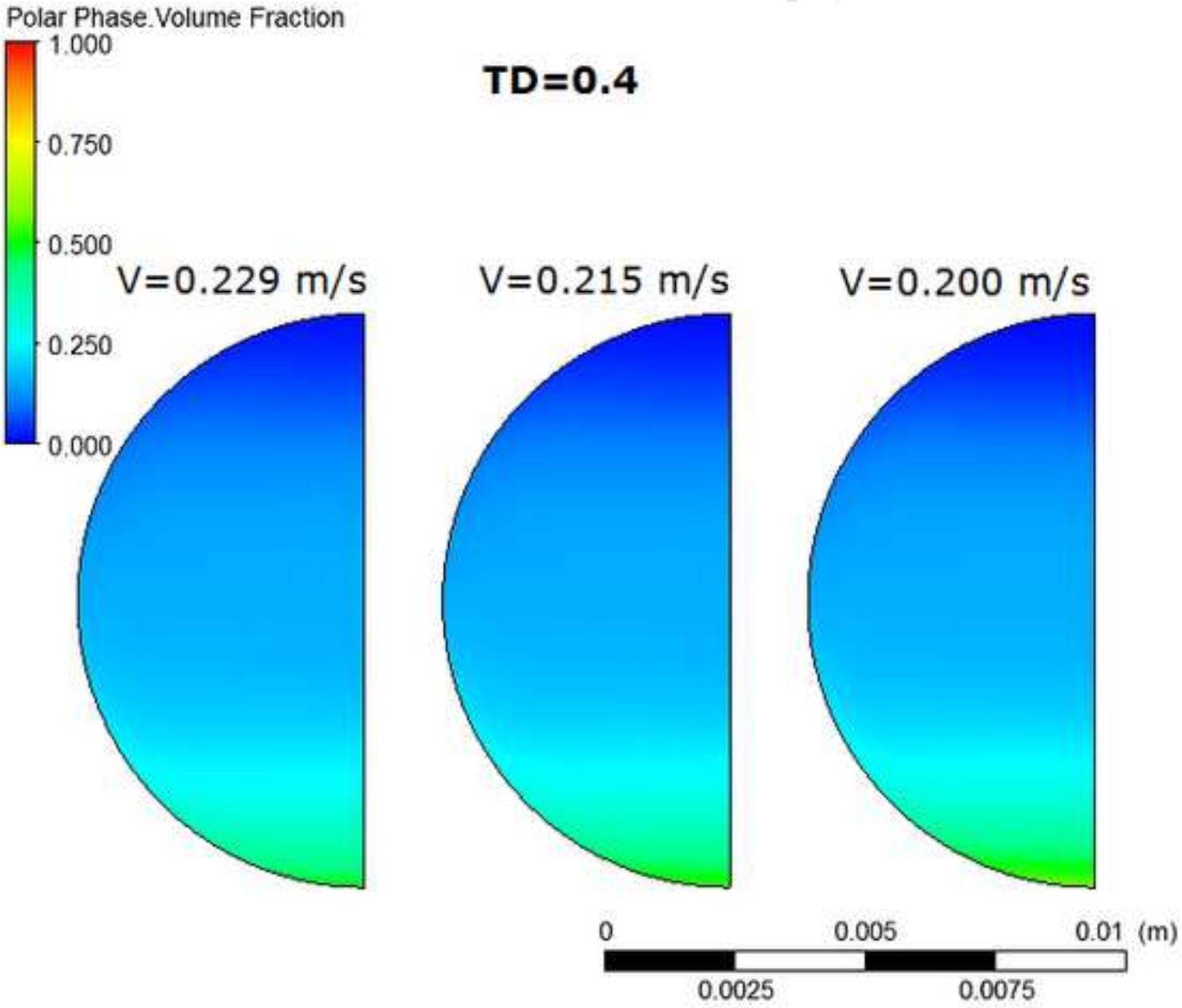
Polar Phase.Volume Fraction
1.000
0.750
0.500
0.250
0.000
TD=0.4
V=0.229 m/s
V=0.215 m/s
V=0.200 m/s
0
0.005
0.01 (m)
0.0025
0.0075

Figure(s)

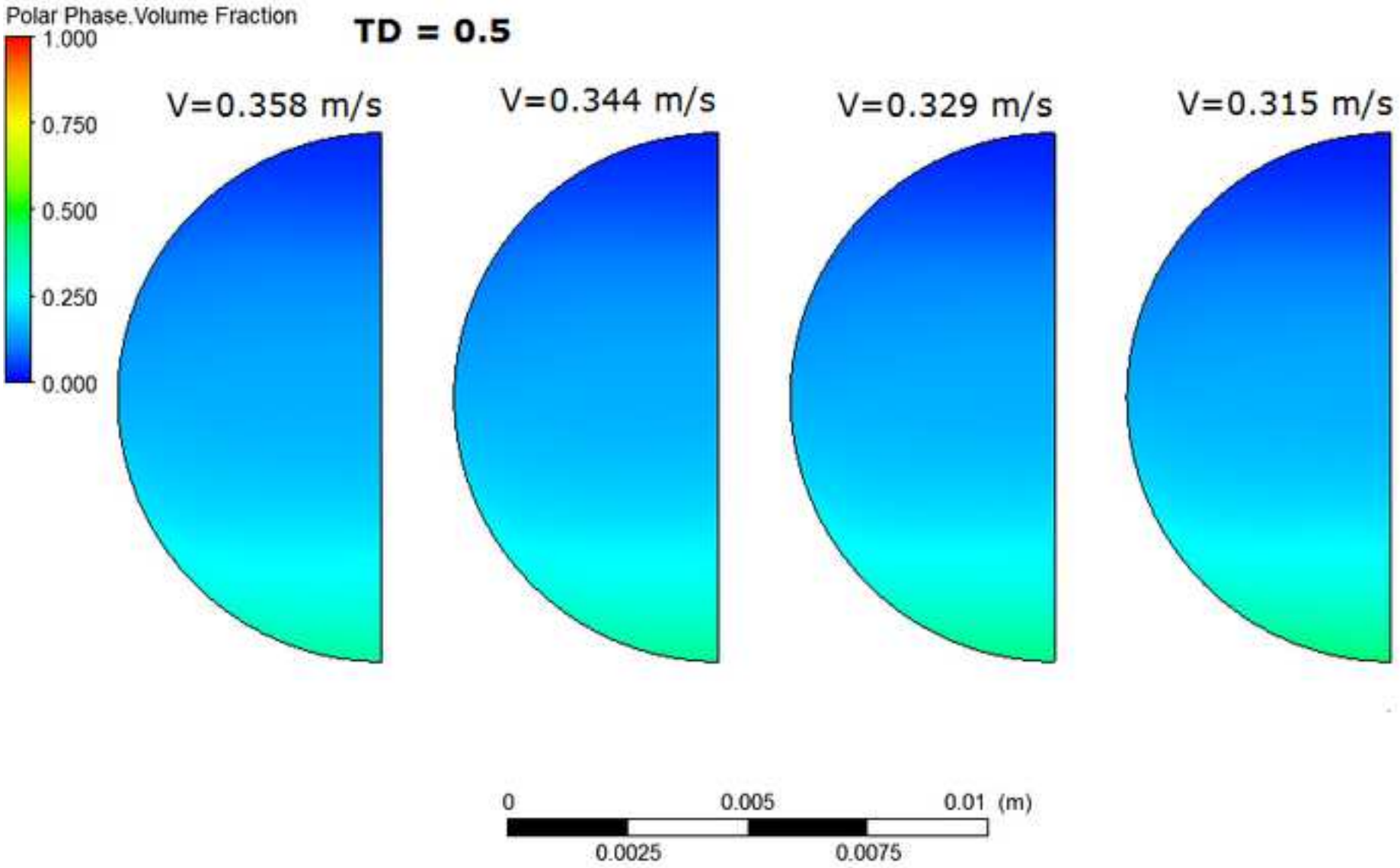
Polar Phase.Volume Fraction
1.000
0.750
0.500
0.250
0.000
TD = 0.5
V=0.358 m/s
V=0.344 m/s
V=0.329 m/s
V=0.315 m/s
0
0.005
0.01 (m)
0.0025
0.0075

Figure(s)

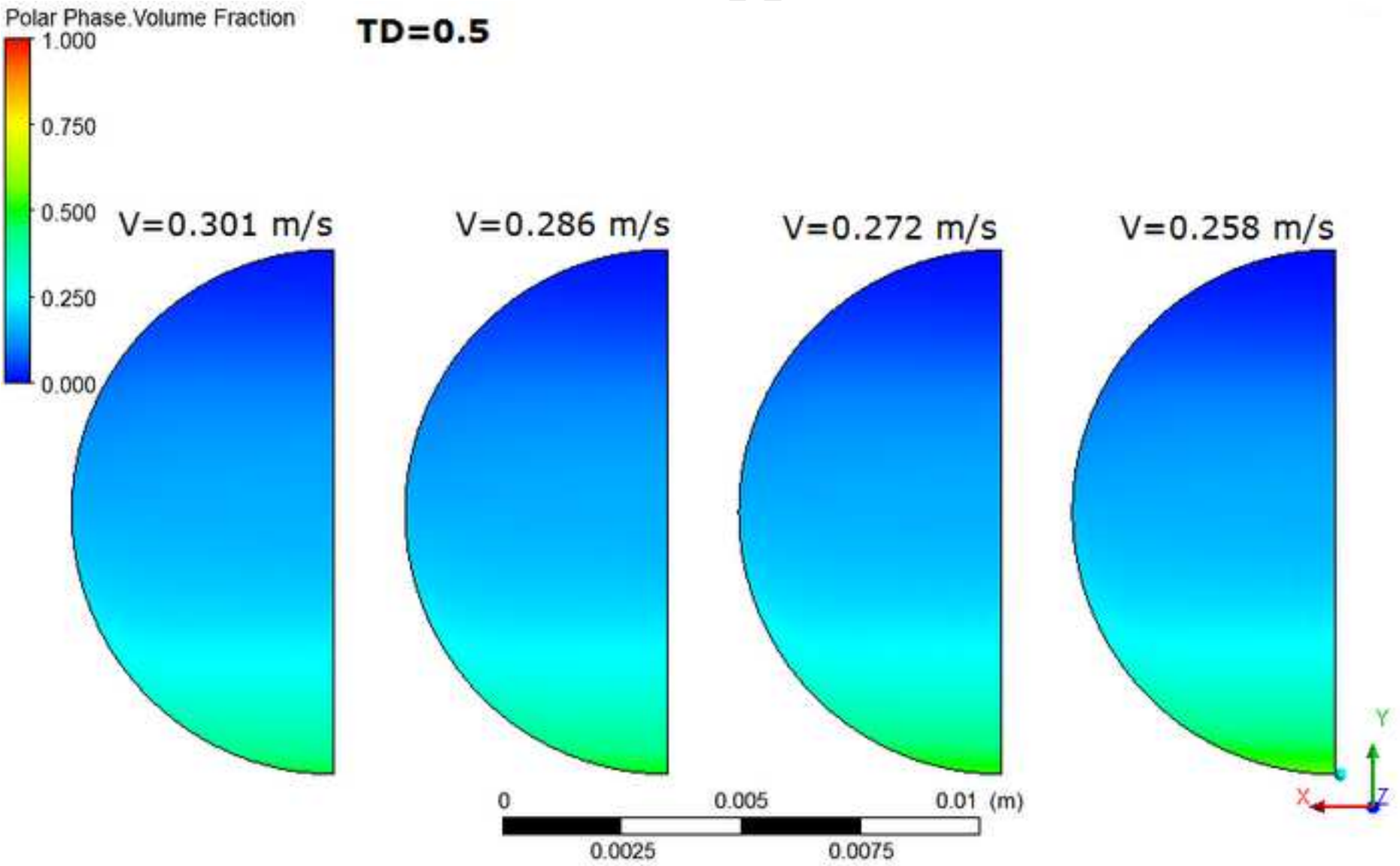
Polar Phase.Volume Fraction
1.000
0.750
0.500
0.250
0.000
TD=0.5
V=0.301 m/s
V=0.286 m/s
V=0.272 m/s
V=0.258 m/s
0
0.005
0.01 (m)
0.0025
0.0075
Y
X
Z